

1 Secondary organic aerosol enhanced by increasing atmospheric oxidizing capacity in  
2 Beijing-Tianjin-Hebei (BTH), China

3  
4 Tian Feng<sup>1,2,6</sup>, Shuyu Zhao<sup>1,3</sup>, Naifang Bei<sup>4</sup>, Jiarui Wu<sup>1,3</sup>, Suixin Liu<sup>1,3</sup>, Xia Li<sup>1,3</sup>, Lang Liu<sup>1,3</sup>, Yang Qian<sup>7</sup>,  
5 Qingchuan Yang<sup>3</sup>, Yichen Wang<sup>3</sup>, Weijian Zhou<sup>1,5,6</sup>, Junji Cao<sup>1,3,5</sup>, Guohui Li<sup>1,3,5\*</sup>  
6

7 <sup>1</sup>State Key Laboratory of Loess and Quaternary Geology, Institute of Earth Environment, Chinese Academy of  
8 Sciences, Xi'an, China

9 <sup>2</sup>Department of Geography & Spatial Information Techniques, Ningbo University, Ningbo, China

10 <sup>3</sup>Key Laboratory of Aerosol Chemistry and Physics, Institute of Earth Environment, Chinese Academy of  
11 Sciences, Xi'an, China

12 <sup>4</sup>School of Human Settlements and Civil Engineering, Xi'an Jiaotong University, Xi'an, China

13 <sup>5</sup>CAS Center for Excellence in Quaternary Science and Global Change, Xi'an, China

14 <sup>6</sup>Xi'an Accelerator Mass Spectrometry Center, Xi'an, China

15 <sup>7</sup>State Key Laboratory of Environmental Criteria and Risk Assessment & Environmental Standards Institute,  
16 Chinese Research Academy of Environmental Sciences, Beijing, China

17  
18 *Correspondence to:* Guohui Li (ligh@ieecas.cn)  
19

20 **Abstract.** The implementation of the Air Pollution Prevention and Control Action Plan in  
21 China since 2013 has profoundly altered the ambient pollutants in the Beijing-Tianjin-Hebei  
22 region (BTH). Here we show observations of substantially increased O<sub>3</sub> concentrations  
23 (about 30%) and a remarkable increase in the ratio of organic carbon (OC) to elemental  
24 carbon (EC) in BTH during the autumn from 2013 to 2015, revealing an enhancement in  
25 atmospheric oxidizing capacity (AOC) and secondary organic aerosol (SOA) formation. To  
26 explore the impacts of increasing AOC on the SOA formation, a severe air pollution episode  
27 from 3 to 8 October 2015 with high O<sub>3</sub> and PM<sub>2.5</sub> concentrations is simulated using the  
28 WRF-Chem model. The model performs reasonably well in simulating the spatial  
29 distributions of PM<sub>2.5</sub> and O<sub>3</sub> concentrations over BTH and the temporal variations of PM<sub>2.5</sub>,  
30 O<sub>3</sub>, NO<sub>2</sub>, OC, and EC concentrations in Beijing compared to measurements. Sensitivity  
31 studies show that the change in AOC substantially influences the SOA formation in BTH. A  
32 sensitivity case characterized by a 31% O<sub>3</sub> decrease (or 36% OH decrease) reduces the SOA  
33 level by about 30% and the SOA fraction in total organic aerosol by 17% (from 0.52 to 0.43,  
34 dimensionless). Spatially, the SOA decrease caused by reduced AOC is ubiquitous in BTH,  
35 but the spatial relationship between SOA concentrations and the AOC is dependent on the  
36 SOA precursor distribution. Studies on SOA formation pathways further show that, when the  
37 AOC is reduced, the SOA from oxidation and partitioning of semi-volatile POA and  
38 co-emitted intermediate volatile organic compounds (IVOCs) decreases remarkably, followed  
39 by those from anthropogenic and biogenic VOCs. Meanwhile, the SOA decrease in the  
40 irreversible uptake of glyoxal and methylglyoxal on aerosol surfaces is negligible.

41

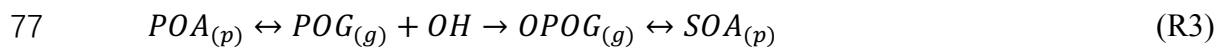
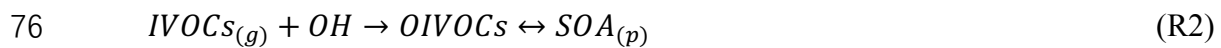
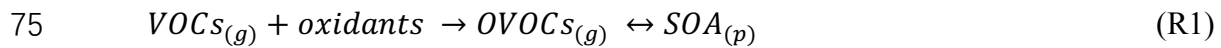
## 42 1 Introduction

43 Severe haze pollutions characterized by exceedingly high concentrations of fine  
44 particulate matter (PM<sub>2.5</sub>) in Beijing-Tianjin-Hebei (BTH), China have drawn much attention  
45 from the public, government, and science community (Han et al., 2014; Jiang et al., 2015; Li  
46 et al., 2017a; Quan et al., 2014; Wang et al., 2016a). Elevated levels of PM<sub>2.5</sub> concentrations  
47 not only deteriorate air quality and visibility (Cao et al., 2012a; Feng et al., 2016; Seinfeld  
48 and Pandis, 2006), but also threaten public health and ecosystem (Cao et al., 2012b; Tie et  
49 al., 2016). In addition, PM<sub>2.5</sub> also modulates the energy budget of the earth system directly  
50 through absorbing and scattering the incident solar radiation and indirectly via acting as cloud  
51 condensation nuclei (CCN) and ice nuclei (IN) and subsequently altering cloud albedo and  
52 lifetime (Li et al., 2008; 2009; Wang et al., 2013; 2016b; 2018; Zhou et al., 2017).

53 Organic aerosol (OA) is a key component of PM<sub>2.5</sub> in ambient air, constituting of 20~90%  
54 of the PM<sub>2.5</sub> mass concentration (Kanakidou et al., 2005; Zhang et al., 2007). Previous studies  
55 have confirmed a large mass fraction of OA in ambient PM<sub>2.5</sub> in various Chinese cities. For  
56 example, Huang et al. (2014) have reported that OA accounts for 30~50% of the total PM<sub>2.5</sub>  
57 mass in megacities in China (e.g., Beijing, Shanghai, Guangzhou, and Xi'an) during severe  
58 haze episodes. Positive matrix factorization (PMF) analyses of the aerosol chemical  
59 speciation monitor (ACSM) measurements in Beijing have shown that OA contributes 40%  
60 and 52% of refractory submicron particulate matters in summer 2011 and winter 2012,  
61 respectively (Sun et al., 2013; 2012). Over BTH, Huang et al. (2017) have demonstrated that  
62 OA constitutes the most important part in the major chemical components of gravimetric  
63 PM<sub>2.5</sub> (20~25%) based on measurements at 3 urban sites from June 2014 to April 2015.

64 OA is traditionally categorized into primary and secondary organic aerosols (referred to  
65 as POA and SOA, respectively) in terms of its source and formation in the atmosphere. POA  
66 is the OA directly emitted into the atmosphere, and SOA is formed through a series of

67 chemical conversions of precursors and gas-particle partitioning, closely associated with the  
68 abundance of oxidants in the atmosphere and ambient temperature (Feng et al., 2016; Li et al.,  
69 2011b; Tsimpidi et al., 2010). SOA precursors mainly include volatile organic compounds  
70 (VOCs) emitted from anthropogenic and biogenic sources (Odum et al., 1996; Pankow, 1994),  
71 primary organic gases (POG) emitted or formed in the evaporation of POA, and intermediate  
72 VOCs (IVOCs) co-emitted with the POA (Lipsky and Robinson, 2006; Robinson et al., 2007;  
73 Shrivastava et al., 2006). The pathway of SOA formation is illustrated as follows (Li et al.,  
74 2011b; Robinson et al., 2007):



78 where the subscript  $g$  and  $p$  denote gas- and particle-phase, respectively. OVOCs, OIVOCs,  
79 and OPOG are oxidized VOCs, IVOCs, and POG, respectively. The oxidants in the chemical  
80 reactions mainly include ozone ( $O_3$ ), hydroxyl radical (OH) and nitrate radical ( $NO_3$ ).  
81 Apparently, the abundance of oxidants in the atmosphere plays an important role in the SOA  
82 formation, and increasing oxidants potentially enhance SOA formation. It is worth noting that  
83 heterogeneous reactions also play a considerable role in SOA formation (Fu et al., 2009; Li et  
84 al., 2011b).

85 Over the last decade,  $O_3$  concentrations have dramatically increased in eastern China. For  
86 example, Cheng et al. (2016) have reported an increasing trend of the daily maximum 1h  $O_3$   
87 concentration over Beijing from 2004 to 2015. Ma et al. (2016) have observed a significant  
88 increase of surface  $O_3$  concentrations at a rural station in the north of eastern China from  
89 2003 to 2015. Since 2013, the implementation of the Air Pollution Prevention and Control  
90 Action Plan (APPCAP) in China have profoundly altered the air pollutants in BTH (He et al.,  
91 2017; Li et al., 2017b; Wu et al., 2017). He et al. (2017) have reported that the ambient OA

92 concentration has been significantly reduced by 27.5%, 17.4%, and 14.0% in Beijing, Tianjin,  
93 and Hebei, respectively, from 2013 to 2017. The increasing O<sub>3</sub> concentration has become a  
94 new culprit for the deterioration of the air quality in eastern China (Li et al., 2017b; Wu et al.,  
95 2017). Li et al. (2017b) have reported that the O<sub>3</sub> concentration has increased by 10% from  
96 2013 to 2015 averaged over 65 cities of eastern China during April ~ September. In Beijing,  
97 the summertime O<sub>3</sub> concentration has increased by 23% from 2013 to 2015 (Wu et al., 2017).  
98 Such an increasing trend of O<sub>3</sub> concentrations reflects an enhancement of the atmospheric  
99 oxidizing capacity (AOC), which, as expected, potentially influences the SOA formation and  
100 OA components. Therefore, it is imperative to evaluate the impact of the increasing AOC on  
101 the SOA formation over BTH.

102 The objective of this study is to evaluate the impact of the increasing AOC on OA  
103 components in BTH (Figure 1) during a haze episode in the autumn of 2015 using the  
104 WRF-Chem model. Model and configuration are described in Sect. 2; the results and  
105 discussion are presented in Sect. 3. The conclusions are drawn in Sect. 4.

106

## 107 **2 Model and method**

### 108 **2.1 WRF-Chem model and configuration**

109 In this study, simulations are performed using a specific version of the WRF-Chem  
110 model (Grell et al., 2005) developed by Li et al. (2011b; 2011a; 2012; 2010). The model  
111 includes a flexible gas phase chemical module and the Models-3 community multiscale air  
112 quality (CMAQ) aerosol module (Binkowski and Roselle, 2003). The photolysis rates are  
113 calculated using the FTUV module (Li et al., 2005; Tie et al., 2003) which takes into account  
114 the effects of clouds and aerosols on photochemistry. A non-traditional SOA module based on  
115 the volatility basis-set (VBS) method (Donahue et al., 2006; Robinson et al., 2007) is  
116 incorporated into the model to simulate organic aerosols. In this module, POA is distributed

117 in logarithmically spaced volatility bins and presumed to be semi-volatile and  
118 photochemically reactive (Li et al., 2011b). The module uses 9 surrogate species with  
119 saturation concentration ranging from  $10^{-2}$  to  $10^6$   $\mu\text{g m}^{-3}$  at room temperature to represent  
120 POA compositions (Shrivastava et al., 2008). IVOCs, co-emitted with the POA but in the gas  
121 phase, are also oxidized by OH to form SOA. In addition, the SOA formation from glyoxal  
122 and methylglyoxal is included in the module, which is parameterized as a first-order  
123 irreversible uptake on aerosol surface with a reactive uptake coefficient of  $3.7 \times 10^{-3}$   
124 (Volkamer et al., 2007; Zhao et al., 2006). Inorganic aerosols are calculated by the  
125 ISORROPIA version 1.7 (Nenes et al., 1998). The GOCART (Georgia Tech/Goddard Global  
126 Ozone Chemistry Aerosol Radiation and Transport model) dust module is used to estimate  
127 the emission, transport, dry deposition, and gravitational settling of dust (Ginoux et al., 2001).  
128 The biomass burning emissions are from the Fire Inventory from NCAR (FINN)  
129 (Wiedinmyer et al., 2011; 2006). The dry deposition of chemical species is parameterized  
130 following Wesely (1989) and the wet deposition is calculated using the method in the CMAQ  
131 module (Binkowski and Roselle, 2003). Specifically, the surface and upper air observational  
132 wind fields from China Meteorological Administration (CMA) during the study period are  
133 assimilated using the four-dimensional data assimilation (FDDA) method to better simulate  
134 meteorological fields.

135 A severe haze episode from 3 to 8 October 2015 in BTH with high  $\text{O}_3$  and  $\text{PM}_{2.5}$   
136 concentrations is simulated. The model is configured with one single domain which is  
137 centered at  $116^\circ\text{E}$  and  $38^\circ\text{N}$  with grid spacing of  $6 \text{ km} \times 6 \text{ km}$  ( $200 \times 200$  grid cells).  
138 Thirty-five stretched vertical levels with spacing ranging from about 30 m near surface, to  
139 500 m at 2.5 km, and 1 km above 14 km are used in the model configuration. The monthly  
140 average anthropogenic emission inventory is developed by Zhang et al. (2009) and Li et al.  
141 (2017c), with the base year of 2013, including agriculture, industry, power generation,

142 residential, and transportation sources. The temporal resolution of emissions used in  
143 simulations is 1 hour, and the temporal allocation for different sources follows those in Zhang  
144 et al. (2009). Figure 2 presents the spatial distributions of anthropogenic volatile organic  
145 compounds (VOCs) and organic carbon (OC) emissions in October, showing high emissions  
146 in urban areas. The emissions of various species in Beijing, Tianjin, Hebei, and the entire  
147 domain in October 2015 are summarized in Table 1. Biogenic emissions are calculated online  
148 using the MEGAN (Model of Emissions of Gases and Aerosol from Nature) model (Guenther  
149 et al., 2006). The model configuration is presented in Table 2.

## 150 **2.2 Pollutant measurements**

151 Measurement data used in this study include the hourly concentrations of O<sub>3</sub>, NO<sub>2</sub>, SO<sub>2</sub>,  
152 CO, and PM<sub>2.5</sub> from ambient monitoring stations of China's Ministry of Environment and  
153 Ecology (China MEE) and hourly OC and EC concentrations in PM<sub>2.5</sub> measured hourly at  
154 Chinese Research Academy of Environmental Sciences (CRAES) using a Sunset OC/EC  
155 Analyzer (RT-4, Sunset Lab, USA). The OC/EC analyzer has been widely used in ambient  
156 and indoor OC/EC detections in China (Liu et al., 2018; Wei et al., 2014). In addition, hourly  
157 submicron POA and SOA concentrations are obtained from the ACSM measurement  
158 analyzed using the PMF method at National Center for Nanoscience and Technology (NCNT)  
159 in Beijing.

## 160 **2.3 Model simulations**

161 We define the simulation with the AOC in October 2015 as the reference (REF). The  
162 model result in REF is compared with the observations to evaluate the model performance.  
163 To examine the impact of increasing AOC on OA components, we perform 4 sensitivity  
164 experiments (SEN1~4) by varying AOC. Compared with the REF simulation, we decrease all  
165 the photolysis frequencies by 10%, 20%, 30%, and 40%, respectively, in the model  
166 simulations.

## 167 2.4 Statistic method

168 The mean bias (MB), normalized mean bias (NMB), root mean square error (RMSE),  
169 index of agreement (IOA), and linear Pearson correlation coefficient ( $r$ ) are selected to  
170 evaluate the WRF-Chem model simulations against observations.

$$171 \quad MB = \frac{1}{N} \sum_{i=1}^N (P_i - O_i) \quad (1)$$

$$172 \quad NMB = \frac{\sum_{i=1}^N (P_i - O_i)}{\sum_{i=1}^N O_i} \times 100\% \quad (2)$$

$$173 \quad RMSE = \left[ \frac{1}{N} \sum_{i=1}^N (P_i - O_i)^2 \right]^{\frac{1}{2}} \quad (3)$$

$$174 \quad IOA = 1 - \frac{\sum_{i=1}^N (P_i - O_i)^2}{\sum_{i=1}^N (|P_i - \bar{P}| + |O_i - \bar{O}|)^2} \quad (4)$$

$$175 \quad r = \frac{\sum_{i=1}^N (P_i - \bar{P})(O_i - \bar{O})}{\sqrt{\sum_{i=1}^N (P_i - \bar{P})^2} \sqrt{\sum_{i=1}^N (O_i - \bar{O})^2}} \quad (5)$$

176 where  $P_i$  and  $O_i$  are the simulated and observed variables, respectively.  $N$  is the total  
177 number of predictions.  $\bar{P}$  and  $\bar{O}$  denote the average of predictions and observations,  
178 respectively. IOA ranges from 0 to 1 theoretically, with 1 suggesting perfect agreement  
179 between predictions and observations.

180

## 1812 3 Results and discussion

### 182 3.1 Observed increasing O<sub>3</sub> concentration and OC/EC ratio

183 Figure 3a shows the annual variation of measured mean concentrations of O<sub>3</sub>, NO<sub>2</sub>, SO<sub>2</sub>,  
184 CO, and PM<sub>2.5</sub> over BTH in the autumn from 2013 to 2017. To better present the pollution  
185 characteristics in autumn, the observations from 15 September to 14 November are selected  
186 in this study, which avoids the heating period (starting from 15 November) in northern China.  
187 Obvious decreasing trends in NO<sub>2</sub>, SO<sub>2</sub>, CO, and PM<sub>2.5</sub> concentrations during recent years  
188 are observed since the implementation of APPCAP (Figure 3a). The O<sub>3</sub> concentration,  
189 however, has increased by about 30% during the same period. Such an O<sub>3</sub> increase indicates a

190 considerable enhancement of the AOC, considering the controlling role of O<sub>3</sub> in the AOC in  
191 the troposphere (Brasseur et al., 1999). The reason for the AOC or O<sub>3</sub> increase since 2013  
192 still remains elusive. Li et al. (2018) have proposed that the O<sub>3</sub> increase in China since 2013  
193 is associated with the decreased removal efficiency of HO<sub>x</sub> (OH + peroxy) on aerosol  
194 surfaces caused by the reduced aerosol concentrations since the implementation of APPCAP.  
195 However, further studies need to be conducted to evaluate the O<sub>3</sub> contribution of the  
196 photolysis change caused by the aerosol-radiation interaction and aerosol-cloud interaction  
197 induced by decreasing aerosols in China.

198 As important PM<sub>2.5</sub> components, organic carbon (OC) and elemental carbon (EC) are  
199 measured in Beijing in the autumns from 2013 to 2015 (Figure 3b). The measured OC/EC  
200 ratio has substantially increased during the 3 years (about 44%). There are two possible  
201 reasons for this. Firstly, the increase might be attributed, at least in part, to the increasing  
202 AOC, which enhances the SOA formation. Secondly, the increase might be caused by the  
203 changes in OC and EC emissions due to the implementation of APPCAP. The large  
204 variability in OC and EC concentrations in Figure 3b suggests considerable emission changes,  
205 although it is still difficult to evaluate exactly how much the emissions have been changed.  
206 Since SOA formation is closely associated with the abundance of oxidants (Li et al., 2011b;  
207 Robinson et al., 2007), OA in BTH is expected to be more oxygenated (add oxygen) and  
208 hence to increase in mass with enhanced AOC.

## 209 **3.2 Model evaluation**

### 210 **3.2.1 Meteorological fields**

211 Model performance in meteorological fields is crucial for the simulation of air pollutants  
212 (Bei et al., 2010; 2012; 2017). Figures 4 and 5 present the simulated temporal variations of  
213 the surface temperature, relative humidity, wind speed, and wind direction against  
214 observations at 4 meteorological stations (Beijing, Tianjin, Shijiazhuang, and Baoding,



215 Figure 1) in BTH.

216 The model performs well in reproducing the observed diurnal cycles of the surface  
217 temperature and relative humidity at the 4 stations (Figure 4). The simulated temporal  
218 variations of temperature and relative humidity are in good agreement with the observations  
219 at the meteorological station in Tianjin. However, in the other 3 cities, the model generally  
220 cannot well reproduce the fairly low temperature and high relative humidity during nighttime.  
221 In general, the model replicates the low winds during 3-7 October in Beijing, Tianjin, and  
222 Baoding, but slightly overestimates the wind speed in Shijiazhuang, particularly in the  
223 morning of 8 October (Figure 5). The model fails to produce the occurrence of the strong  
224 wind with a maximum speed exceeding  $10 \text{ m s}^{-1}$  and the wind direction at noon on 8 October  
225 in Beijing. Overall, the model still generally captures the temporal variations of wind  
226 directions in the 4 cities.

### 227 **3.2.2 PM<sub>2.5</sub>, O<sub>3</sub>, and NO<sub>2</sub>**

228 The spatial distributions of simulated and observed daily PM<sub>2.5</sub> concentration during the  
229 period from 3 to 8 October 2015 are presented in Figure 6 along with wind fields. This haze  
230 event in BTH can be divided into 4 stages: (1) startup (3 October), (2) development (4  
231 October), (3) maturation (5-7 October), and (4) dissipation (8 October). On 3 October, the  
232 haze formed in Shandong and southern BTH, accompanied by weak winds near the surface  
233 ( $< 2 \text{ m s}^{-1}$ ). On 4 October, the southerly wind prevailed, causing trans-boundary transport of  
234 air pollutants from south to north, and the PM<sub>2.5</sub> concentration in BTH rapidly increased.  
235 From 5 to 7 October, the southerly wind continued and the haze became persistently severe in  
236 BTH. Finally, a strong northerly wind cleaned up the haze within several hours on 8 October.  
237 The model reasonably reproduces the haze evolution in BTH, but it generally underestimates  
238 the PM<sub>2.5</sub> concentration in Shandong province.

239 Figure 7 shows the observed and simulated spatial distribution of peak O<sub>3</sub> concentrations

240 at 14:00 (local time, hereafter) during the episode. Similar to PM<sub>2.5</sub>, the high O<sub>3</sub> concentration  
241 first occurred in Shandong province on 3 October, and propagated to BTH on 4 October.  
242 During the maturation period, the O<sub>3</sub> level in BTH still remained high. The simulated spatial  
243 distributions of O<sub>3</sub> concentrations generally agree well with the observations during the four  
244 stages, but underestimation or overestimation still exists.

245 Figure 8 shows the temporal variations of the simulated and observed surface PM<sub>2.5</sub>, O<sub>3</sub>,  
246 and NO<sub>2</sub> concentrations averaged over 12 ambient monitoring stations in Beijing. The  
247 simulated and observed PM<sub>2.5</sub> temporal pattern clearly shows the 4 stages of the haze episode,  
248 with the PM<sub>2.5</sub> concentration increasing from about 20 µg m<sup>-3</sup> during the startup stage to more  
249 than 300 µg m<sup>-3</sup> during the maturation stage. The model generally replicates the evolution of  
250 the observed PM<sub>2.5</sub> concentration with an IOA (*r*) of 0.95 (0.91), but slightly underestimates  
251 the PM<sub>2.5</sub> concentration with an MB (NMB) of -13.0 µg m<sup>-3</sup> (-8.7%). The simulated diurnal  
252 profile of the O<sub>3</sub> concentration is well consistent with observations, with an IOA (*r*) of 0.94  
253 (0.92), but the model overestimates the O<sub>3</sub> diurnal lows during the maturation stage.  
254 Additionally, Figures 8a and 8b also show that both O<sub>3</sub> and PM<sub>2.5</sub> pollutions occur during the  
255 maturation stage in Beijing, as previously reported for non-winter seasons (Jia et al., 2017).  
256 The model also exhibits good performance in simulating the temporal variation of NO<sub>2</sub>  
257 concentrations, with an IOA (*r*) of 0.90 (0.81).

### 258 **3.2.3 Carbonaceous aerosols**

259 The simulated carbonaceous aerosols including POA, SOA, and EC in the model are  
260 compared with the hourly observations in Beijing (Figure 9). In general, the temporal  
261 variations of the measured carbonaceous aerosols are similar to that of the PM<sub>2.5</sub> in Figure 8a.  
262 The model yields the increasing trend of the POA concentration from the startup to  
263 maturation stages compared to the measurements, but cannot well capture the observed spiky  
264 peaks, with an IOA (*r*) of 0.75 (0.58). Figure 9b shows that the observed SOA concentration

265 is remarkably enhanced during the maturation stage, ranging from 30 to 90  $\mu\text{g m}^{-3}$ , which is  
266 well predicted by the model. The MB, NMB, IOA, and  $r$  for the simulated SOA concentration  
267 are -2.1  $\mu\text{g m}^{-3}$ , -6.9%, 0.89, and 0.81, respectively. Although the IOA and  $r$  for the simulated  
268 EC concentration reach 0.92 and 0.90, respectively, the model considerably underestimates  
269 the EC concentration against measurement on October 6 and 7, which is likely caused by the  
270 variation in the anthropogenic emissions.

271 Overall, the model performs reasonably in reproducing the observed meteorological  
272 fields and the  $\text{PM}_{2.5}$  and  $\text{O}_3$  evolutions, and temporal variations of carbonaceous aerosols  
273 during the pollution episode, providing a reliable base for the further sensitivity studies.

### 274 **3.3 Impact of increasing oxidizing capacity on OA**

275 Compared to the REF simulation, when the photolysis frequencies are decreased by 10%,  
276 20%, 30%, and 40% in the 4 sensitivity experiments (SEN1~4), respectively, the  $\text{O}_3$  (OH  
277 radical) concentration is correspondingly reduced by 7.4% (9.2%), 15.1% (18.3%), 22.9%  
278 (26.9%), and 30.9% (35.7%). It is worth noting that the REF experiment is assumed to  
279 represent a situation in autumn with the high AOC, and the SEN1~4 experiments could be  
280 regarded as 4 scenarios with the different lower AOC.

#### 281 **3.3.1 OA component changes**

282 Figures 10a and 10b show the variation of POA, SOA, and TOA concentrations as a  
283 function of the  $\text{O}_3$  and OH concentration changes over BTH by differentiating REF and the 4  
284 sensitivity experiments, respectively. The SOA level decreases almost linearly with  
285 decreasing  $\text{O}_3$  or OH concentrations, indicating that the AOC plays an important role in the  
286 SOA formation over BTH. In the SEN4 experiment with the most reduction of the AOC, the  
287 SOA concentration in BTH is reduced by 31.3% or 5.2  $\mu\text{g m}^{-3}$  on average during the episode.  
288 The reduction in POA level with decreasing  $\text{O}_3$  and OH concentrations is generally not  
289 substantial, indicating that IVOCs and VOCs are the most important SOA contributors. The

290 TOA (sum of POA and SOA) level also exhibits a decreasing trend with O<sub>3</sub> and OH  
291 concentrations. In Figures 10c and 10d, the SOA mass fraction in TOA and OC/EC ratio is  
292 considerably reduced as the AOC decreases. The SOA fraction (OC/EC ratio) is about 0.52  
293 (6.39) in the REF simulation and almost linearly decreases to around 0.43 (5.49) in the SEN4  
294 experiment, indicating a slower aging process of OA with decreasing AOC. The simulated  
295 decrease in OC/EC ratio due to reduced AOC could interpret the observed change in OC/EC  
296 ratio in Figure 3b to some degree.

297 It is worth noting that the increase in OC/EC ratio potentially influences atmospheric  
298 radiation and thermodynamical profiles, through enhancing aerosol scattering and absorption  
299 simultaneously (Wang et al., 2013). When the photolysis frequencies are reduced by 30% in  
300 the SEN3 experiment, compared to the REF, the downward shortwave radiation is reduced by  
301 1.2 W m<sup>-2</sup> on average in BTH, and the surface temperature is decreased by around 0.016 °C  
302 during daytime. Effects of the AOC change on the temperature profile is not significant, and  
303 the daytime temperature decrease in the SEN3 experiment is less than 0.005 °C within 1 km  
304 height from surface.

### 305 **3.3.2 SOA spatial change in SEN3**

306 Among the 4 experiments, the O<sub>3</sub> change over BTH in SEN3 is close to the observed  
307 change (about 30% increase, Figure 3a). Therefore, we further analyze the SOA spatial  
308 change in the SEN3 experiment. To illustrate the impacts of the AOC change on the spatial  
309 distribution of SOA concentrations in BTH during the haze episode, Figure 11 shows the  
310 spatial distributions of the variation in the main oxidant (OH) and SOA concentrations  
311 averaged from 4 to 7 October by differentiating REF and the SEN3 experiment. When the  
312 photolysis rates are reduced by 30%, the OH concentration over BTH is generally decreased  
313 by more than 20%, but the OH variation distribution is not uniform (Figure 11c). The OH  
314 decrease is remarkable in the west of Hebei province, compared to the other regions of BTH,

315 showing the variety of OH sinks and its reservoirs. The most striking decrease in SOA mass  
316 occurs in Beijing and surrounding areas, exceeding  $8 \mu\text{g m}^{-3}$  (Figure 11b); while the mass  
317 percentage decrease is more noticeable in the west of Hebei province (more than 26%, Figure  
318 11d), which is generally corresponding to the OH reduction. Although OH is the main  
319 oxidant in the SOA formation during daytime, the spatial change of SOA concentration is not  
320 well consistent with that of the OH concentration, especially for the mass change (Figure  
321 11a). The geographical difference probably results from the spatial distribution variation of  
322 anthropogenic and biogenic precursors of SOA. In the middle and east BTH, massive  
323 anthropogenic SOA precursors are emitted from residential, transportation and industrial  
324 sources; while in the west BTH, biogenic precursor emissions are dominant for the SOA  
325 formation, but much less than those from anthropogenic sources in the middle and east BTH  
326 (Figure 2).

### 327 **3.3.3 Changes in the secondary organic aerosol pathways**

328 The spatial decrease in SOA concentration highlights the important influence of AOC  
329 change on the SOA formation over BTH. To understand how the SOA components are  
330 affected by the changing AOC, we further examine the variation of the SOA formation  
331 pathways. The non-traditional SOA module employed in the WRF-Chem model includes 4  
332 SOA formation pathways: oxidation and partitioning of (1) POA treated as semivolatile and  
333 co-emitted IVOCs (PSOA), (2) anthropogenic VOCs (ASOA), and (3) biogenic VOCs  
334 (BSOA), and (4) heterogeneous reactions of glyoxal and methylglyoxal on aerosol surfaces  
335 (HSOA) (Feng et al., 2016; Li et al., 2011b). SOA formation from the 4 pathways in the REF  
336 and 4 sensitivity experiments is analyzed to examine the influence of the changing AOC.

337 Figure 12 shows the changes in SOA concentrations in the 4 sensitivity experiments  
338 compared with the REF simulation in Beijing, Tianjin, and Hebei, respectively. The impact of  
339 AOC reduction on the 4 pathways and the resulting SOA decreases differ markedly from one

340 another. Since the oxidation and partitioning of semivolatile POA and co-emitted IVOCs  
341 contribute the most to the SOA concentration (Feng et al., 2016), the most substantial SOA  
342 decrease occurs in the PSOA, followed by the ASOA and BSOA. The decrease from the  
343 HSOA in the 4 experiments is negligible, because the HSOA is mainly contributed by the  
344 direct emission of glyoxal and methylglyoxal from residential combustion source (Xing et al.,  
345 2019).

346 It should be noted that, the percentage decreases of SOA from the PSOA in Beijing,  
347 Tianjin, and Hebei are comparable (Figure 12b, d, and f), although the mass decrease in  
348 Beijing is apparently larger than that in Tianjin and Hebei, indicating the ubiquitous effect of  
349 AOC on the PSOA over BTH. The SOA decrease from the ASOA in Beijing is more than that  
350 in Tianjin and Hebei, which is likely due to higher and concentrated anthropogenic VOCs  
351 emissions in Beijing. By contrast, the SOA decreases from the BSOA are all rather small, and  
352 compared with Beijing and Hebei, the SOA decrease from BSOA in Tianjin is even less. In  
353 the northwestern part of BTH, the widely distributed forests emit abundant VOCs; whereas  
354 the biogenic VOC emissions in Tianjin are much lower owing to a less vegetation cover. In  
355 the SEN3 experiment, the SOA decreases in the PSOA, ASOA, and BSOA are 28%, 8%, and  
356 1% in Beijing, respectively, and slightly less than those in Tianjin and Hebei.

357

#### 3583 **4 Summary and conclusions**

359 Observations have revealed substantial increase in O<sub>3</sub> concentrations (about 30%) over  
360 BTH and in the ratio of organic carbon (OC) to elemental carbon (EC) in Beijing during the  
361 autumn from 2013 to 2015, indicating enhanced AOC and SOA formation. We simulate a  
362 6-day haze episode in BTH from 3 to 8 October 2015 using the WRF-Chem model, as a case  
363 study, to explore the influence of the increasing AOC on the SOA formation in BTH.

364 Generally, the model performs reasonably well in predicting the temporal variations of

365 the temperature, relative humidity, wind speed and direction at 4 meteorological stations in  
366 BTH. The spatial distributions of PM<sub>2.5</sub> and O<sub>3</sub> concentrations over BTH and the temporal  
367 variations of PM<sub>2.5</sub>, O<sub>3</sub>, NO<sub>2</sub>, and carbonaceous aerosols including POA, SOA, and EC in  
368 Beijing are also well reproduced against measurements.

369 Four sensitivity experiments with different reductions in the AOC show that changing  
370 AOC substantially affects the SOA formation. In the SEN4 scenario, characterized by a 30.9%  
371 (35.7%) decrease in O<sub>3</sub> (OH) concentration, the SOA concentration is reduced by 31.3% and  
372 the SOA mass fraction in TOA is reduced from 0.52 to 0.43. Spatially, the SOA reduction is  
373 ubiquitous over BTH, but the spatial relationship between the SOA concentration and AOC is  
374 dependent on the SOA precursor distribution. Among the 4 pathways of the SOA formation  
375 in the non-traditional SOA module, the largest SOA reduction in the reduced AOC  
376 environment occurs in the PSOA, followed by the ASOA and BSOA. By contrast, the SOA  
377 reduction in the HSOA is negligible.

378 Although the model reasonably reproduces the observed meteorological fields and  
379 chemical species in BTH, model discrepancies still exist, especially for the PM<sub>2.5</sub> simulation  
380 in Shandong. More studies need to be performed to improve the model simulation and  
381 evaluate the impact of AOC change on SOA formation using more accurate meteorological  
382 fields and updated anthropogenic emissions.

383

384

385 *Author contribution.* Guohui Li, as the contact author, provided the ideas and financial  
386 support, verified the conclusions, and revised the paper. Tian Feng conducted a research,  
387 designed the experiments, carried the methodology out, performed the simulation, processed  
388 the data, prepared the data visualization, and prepared the manuscript with contributions from  
389 all authors. Shuyu Zhao and Naifang Bei provided the treatment of meteorological data,

390 analyzed the study data, validated the model performance, and reviewed the manuscript.  
391 Suixin Liu, Yang Qian, Yichen Wang, and Qingchuan Yang provided the observation data  
392 used in the study, synthesized the observation, and reviewed the paper. Jiarui Wu, Xia Li, and  
393 Lang Liu analyzed the initial simulation data, visualized the model results and reviewed the  
394 paper. Weijian Zhou and Junji Cao provided critical reviews pre-publication stage.

395

396

397 *Acknowledgements.* This work is financially supported by the National Key R&D Plan  
398 (Quantitative Relationship and Regulation Principle between Regional Oxidation Capacity of  
399 Atmospheric and Air Quality (2017YFC0210000)) and National Research Program for Key  
400 Issues in Air Pollution Control (DQGG0105). Tian Feng is supported by National Natural  
401 Science Foundation of China (no. 41703127, 41430424, 41661144020).

402

403

404

405

406



407 **References**

- 408 Bei, N., Lei, W., Zavala, M. and Molina, L. T.: Ozone predictabilities due to meteorological  
409 uncertainties in the Mexico City basin using ensemble forecasts, *Atmos. Chem. Phys.*,  
410 10(13), 6295–6309, doi:10.5194/acp-10-6295-2010, 2010.
- 411 Bei, N., Li, G. and Molina, L. T.: Uncertainties in SOA simulations due to meteorological  
412 uncertainties in Mexico City during MILAGRO-2006 field campaign, *Atmos. Chem.*  
413 *Phys.*, 12(23), 11295–11308, doi:10.5194/acp-12-11295-2012, 2012.
- 414 Bei, N., Wu, J., Elser, M., Feng, T., Cao, J., Haddad, El, I., Li, X., Huang, R., Li, Z., Long,  
415 X., Xing, L., Zhao, S., Tie, X., Prévôt, A. S. H. and Li, G.: Impacts of meteorological  
416 uncertainties on the haze formation in Beijing–Tianjin–Hebei (BTH) during wintertime:  
417 a case study, *Atmos. Chem. Phys.*, 17(23), 14579–14591,  
418 doi:10.5194/acp-17-14579-2017, 2017.
- 419 Binkowski, F. S. and Roselle, S. J.: Models-3 Community Multiscale Air Quality (CMAQ)  
420 model aerosol component 1. Model description, *J. Geophys. Res.*, 108(D6), 4183,  
421 doi:10.1029/2001JD001409, 2003.
- 422 Brasseur, G. P., Orlando, J. J. and Tyndall, G. S.: *Atmospheric Chemistry and Global Change*,  
423 Oxford University Press, Cambridge, USA. 1999.
- 424 Cao, J., Wang, Q. Y., Chow, J. C., Watson, J. G., Tie, X. X., Shen, Z. X., Wang, P. and An, Z.  
425 S.: Impacts of aerosol compositions on visibility impairment in Xi'an, China, *Atmos.*  
426 *Environ.*, 59, 559–566, doi:10.1016/j.atmosenv.2012.05.036, 2012a.
- 427 Cao, J., Xu, H., Xu, Q., Chen, B. and Kan, H.: Fine particulate matter constituents and  
428 cardiopulmonary mortality in a heavily polluted Chinese city, *Environ. Health Perspect.*,  
429 120(3), 373–378, doi:10.1289/ehp.1103671, 2012b.
- 430 Chen, F. and Dudhia, J.: Coupling an advanced land surface-hydrology model with the Penn  
431 State-NCAR MM5 modeling system. Part II: Preliminary model validation, *Mon.*  
432 *Weather Rev.*, 129(4), 569–585,  
433 doi:10.1175/1520-0493(2001)129<0569:caalsh>2.0.co;2, 2001.
- 434 Cheng, N., Li, Y., Zhang, D., Chen, T., Sun, F., Chen, C. and Meng, F.: Characteristics of  
435 Ground Ozone Concentration over Beijing from 2004 to 2015: Trends, Transport, and  
436 Effects of Reductions, *Atmos. Chem. Phys. Discuss.*, 1–21, doi:10.5194/acp-2016-508,  
437 2016.
- 438 Chou, M.-D. and Suarez, M. J.: *A solar radiation parameterization for atmospheric studies*,  
439 edited by M. J. Suarez. 1999.
- 440 Chou, M.-D., Suarez, M. J., Liang, X.-Z. and Yan, M. M. H.: *A thermal infrared radiation*  
441 *parameterization for atmospheric studies*, edited by M. J. Suarez. 2001.
- 442 Donahue, N. M., Robinson, A. L., Stanier, C. O. and Pandis, S. N.: Coupled Partitioning,  
443 Dilution, and Chemical Aging of Semivolatile Organics, *Environ. Sci. Technol.*, 40(8),  
444 2635–2643, doi:10.1021/es052297c, 2006.
- 445 Feng, T., Li, G., Cao, J., Bei, N., Shen, Z., Zhou, W., Liu, S., Zhang, T., Wang, Y., Huang,  
446 R.-J., Tie, X. and Molina, L. T.: Simulations of organic aerosol concentrations during  
447 springtime in the Guanzhong Basin, China, *Atmos. Chem. Phys.*, 16(15), 10045–10061,  
448 doi:10.5194/acp-16-10045-2016, 2016.
- 449 Fu, T.-M., Jacob, D. J. and Heald, C. L.: Aqueous-phase reactive uptake of dicarbonyls as a

450 source of organic aerosol over eastern North America, *Atmos. Environ.*, 43(10), 1814–  
451 1822, doi:10.1016/j.atmosenv.2008.12.029, 2009.

452 Ginoux, P., Chin, M., Tegen, I., Prospero, J. M., Holben, B., Dubovik, O. and Lin, S.-J.:  
453 Sources and distributions of dust aerosols simulated with the GOCART model, *J.*  
454 *Geophys. Res.*, 106(D17), 20255–20273, doi:10.1029/2000JD000053, 2001.

455 Grell, G. A., Peckham, S. E., Schmitz, R., McKeen, S. A., Frost, G., Skamarock, W. C. and  
456 Eder, B.: Fully coupled “online” chemistry within the WRF model, *Atmos. Environ.*,  
457 39(37), 6957–6975, doi:10.1016/j.atmosenv.2005.04.027, 2005.

458 Guenther, A., Karl, T., Harley, P., Wiedinmyer, C., Palmer, P. I. and Geron, C.: Estimates of  
459 global terrestrial isoprene emissions using MEGAN (Model of Emissions of Gases and  
460 Aerosols from Nature), *Atmos. Chem. Phys.*, 6(11), 3181–3210,  
461 doi:10.5194/acp-6-3181-2006, 2006.

462 Han, X., Zhang, M., Gao, J., Wang, S. and Chai, F.: Modeling analysis of the seasonal  
463 characteristics of haze formation in Beijing, *Atmos. Chem. Phys.*, 14(18), 10231–10248,  
464 doi:10.5194/acp-14-10231-2014, 2014.

465 He, K., Zhang, Q., Hong, C., Xie, T., Bai, Y., Du, J., Zhao, L., Cai, J., Lin, Y. and Zhou, R.:  
466 Can Beijing, Tianjin and Hebei Achieve Their PM<sub>2.5</sub> Targets by 2017?, *Clean Air*  
467 *Alliance of China*, Beijing. 2017.

468 Hong, S. Y. and Lim, J.: The WRF single-moment 6-class microphysics scheme (WSM6),  
469 *Asia-Pac. J. Atmos. Sci.*, 42(2), 129–151, 2006.

470 Horowitz, L. W., Walters, S., Mauzerall, D. L., Emmons, L. K., Rasch, P. J., Granier, C., Tie,  
471 X., Lamarque, J.-F., Schultz, M. G., Tyndall, G. S., Orlando, J. J. and Brasseur, G. P.: A  
472 global simulation of tropospheric ozone and related tracers: Description and evaluation  
473 of MOZART, version 2, *J. Geophys. Res.*, 108(D24), 4784, doi:10.1029/2002jd002853,  
474 2003.

475 Huang, R.-J., Zhang, Y., Bozzetti, C., Ho, K. F., Cao, J., Han, Y., Daellenbach, K. R., Slowik,  
476 J. G., Platt, S. M., Canonaco, F., Zotter, P., Wolf, R., Pieber, S. M., Bruns, E. A., Crippa,  
477 M., Ciarelli, G., Piazzalunga, A., Schwikowski, M., Abbaszade, G., Schnelle-Kreis, J.,  
478 Zimmermann, R., An, Z., Szidat, S., Baltensperger, U., Haddad, El, I. and Prévôt, A. S.  
479 H.: High secondary aerosol contribution to particulate pollution during haze events in  
480 China, *Nature*, 514(7521), 218–222, doi:10.1038/nature13774, 2014.

481 Huang, X., Liu, Z., Liu, J., Hu, B., Wen, T., Tang, G., Zhang, J., Wu, F., Ji, D., Wang, L. and  
482 Wang, Y.: Chemical characterization and source identification of PM<sub>2.5</sub> at multiple sites  
483 in the Beijing–Tianjin–Hebei region, China, *Atmos. Chem. Phys.*, 17(21), 12941–12962,  
484 doi:10.5194/acp-17-12941-2017, 2017.

485 Janjić, Z. I.: Nonsingular implementation of the Mellor–Yamada level 2.5 scheme in the  
486 NCEP Meso model. 2002.

487 Jia, M., Zhao, T., Cheng, X., Gong, S., Zhang, X., Tang, L., Liu, D., Wu, X., Wang, L. and  
488 Chen, Y.: Inverse Relations of PM<sub>2.5</sub> and O<sub>3</sub> in Air Compound Pollution between Cold  
489 and Hot Seasons over an Urban Area of East China, *Atmosphere-Basel*, 8(3), 59–12,  
490 doi:10.3390/atmos8030059, 2017.

491 Jiang, C., Wang, H., Zhao, T., Li, T. and Che, H.: Modeling study of PM<sub>2.5</sub> pollutant transport  
492 across cities in China's Jing–Jin–Ji region during a severe haze episode in December  
493 2013, *Atmos. Chem. Phys.*, 15(10), 5803–5814, doi:10.5194/acp-15-5803-2015, 2015.

494 Kanakidou, M., Seinfeld, J. H., Pandis, S. N., Barnes, I., Dentener, F. J., Facchini, M. C., Van  
495 Dingenen, R., Ervens, B., Nenes, A., Nielsen, C. J., Swietlicki, E., Putaud, J. P.,  
496 BALKANSKI, Y., Fuzzi, S., Horth, J., Moortgat, G. K., Winterhalter, R., Myhre, C. E.  
497 L., Tsigaridis, K., Vignati, E., Stephanou, E. G. and Wilson, J.: Organic aerosol and  
498 global climate modelling: a review, *Atmos. Chem. Phys.*, 5(4), 1053–1123,  
499 doi:10.5194/acp-5-1053-2005, 2005.

500 Li, G., Bei, N., Cao, J., Huang, R., Wu, J., Feng, T., Wang, Y., Liu, S., Zhang, Q., Tie, X. and  
501 Molina, L. T.: A possible pathway for rapid growth of sulfate during haze days in China,  
502 *Atmos. Chem. Phys.*, 17(5), 3301–3316, doi:10.5194/acp-17-3301-2017, 2017a.

503 Li, G., Bei, N., Cao, J., Wu, J., Long, X., Feng, T., Dai, W., Liu, S., Zhang, Q. and Tie, X.:  
504 Widespread and persistent ozone pollution in eastern China during the non-winter season  
505 of 2015: observations and source attributions, *Atmos. Chem. Phys.*, 17(4), 2759–2774,  
506 doi:10.5194/acp-17-2759-2017, 2017b.

507 Li, G., Bei, N., Tie, X. and Molina, L. T.: Aerosol effects on the photochemistry in Mexico  
508 City during MCMA-2006/MILAGRO campaign, *Atmos. Chem. Phys.*, 11(11), 5169–  
509 5182, doi:10.5194/acp-11-5169-2011, 2011a.

510 Li, G., Lei, W., Bei, N. and Molina, L. T.: Contribution of garbage burning to chloride and  
511 PM<sub>2.5</sub> in Mexico City, *Atmos. Chem. Phys.*, 12(18), 8751–8761,  
512 doi:10.5194/acp-12-8751-2012, 2012.

513 Li, G., Lei, W., Zavala, M., Volkamer, R., Dusanter, S., Stevens, P. and Molina, L. T.:  
514 Impacts of HONO sources on the photochemistry in Mexico City during the  
515 MCMA-2006/MILAGO Campaign, *Atmos. Chem. Phys.*, 10(14), 6551–6567,  
516 doi:10.5194/acp-10-6551-2010, 2010.

517 Li, G., Wang, Y. and Zhang, R.: Implementation of a two-moment bulk microphysics scheme  
518 to the WRF model to investigate aerosol-cloud interaction, *J. Geophys. Res.*, 113(D15),  
519 D15211, doi:10.1029/2007JD009361, 2008.

520 Li, G., Wang, Y., Lee, K.-H., Diao, Y. and Zhang, R.: Impacts of aerosols on the  
521 development and precipitation of a mesoscale squall line, *J. Geophys. Res.*, 114(D17),  
522 D17205, doi:10.1029/2008JD011581, 2009.

523 Li, G., Zavala, M., Lei, W., Tsimpidi, A. P., Karydis, V. A., Pandis, S. N., Canagaratna, M. R.  
524 and Molina, L. T.: Simulations of organic aerosol concentrations in Mexico City using  
525 the WRF-CHEM model during the MCMA-2006/MILAGRO campaign, *Atmos. Chem.  
526 Phys.*, 11(8), 3789–3809, doi:10.5194/acp-11-3789-2011, 2011b.

527 Li, G., Zhang, R., Fan, J. and Tie, X.: Impacts of black carbon aerosol on photolysis and  
528 ozone, *J. Geophys. Res.*, 110(D23), D23206, doi:10.1029/2005JD005898, 2005.

529 Li, K., Jacob, D. J., Liao, H., Shen, L., Zhang, Q. and Bates, K. H.: Anthropogenic drivers of  
530 2013-2017 trends in summer surface ozone in China, *Proc. Natl. Acad. Sci. U.S.A.*, 17,  
531 201812168–6, doi:10.1073/pnas.1812168116, 2018.

532 Li, M., Zhang, Q., Kurokawa, J.-I., Woo, J.-H., He, K., Lu, Z., Ohara, T., Song, Y., Streets, D.  
533 G., Carmichael, G. R., Cheng, Y., Hong, C., Huo, H., Jiang, X., Kang, S., Liu, F., Su, H.  
534 and Zheng, B.: MIX: a mosaic Asian anthropogenic emission inventory under the  
535 international collaboration framework of the MICS-Asia and HTAP, *Atmos. Chem.  
536 Phys.*, 17(2), 935–963, doi:10.5194/acp-17-935-2017, 2017c.

537 Lipsky, E. M. and Robinson, A. L.: Effects of Dilution on Fine Particle Mass and Partitioning  
538 of Semivolatile Organics in Diesel Exhaust and Wood Smoke, *Environ. Sci. Technol.*,

539 40(1), 155–162, doi:10.1021/es050319p, 2006.

540 Liu, W., Shen, G., Chen, Y., Shen, H., Huang, Y., Li, T., Wang, Y., Fu, X., Tao, S., Liu, W.,  
541 Huang-Fu, Y., Zhang, W., Xue, C., Liu, G., Wu, F. and Wong, M.: Air pollution and  
542 inhalation exposure to particulate matter of different sizes in rural households using  
543 improved stoves in central China, *J. Environ. Sci.*, 63, 87–95,  
544 doi:10.1016/j.jes.2017.06.019, 2018.

545 Ma, Z., Xu, J., Quan, W., Zhang, Z., Lin, W. and Xu, X.: Significant increase of surface  
546 ozone at a rural site, north of eastern China, *Atmos. Chem. Phys.*, 16(6), 3969–3977,  
547 doi:10.5194/acp-16-3969-2016, 2016.

548 Nenes, A., Pandis, S. N. and Pilinis, C.: ISORROPIA: A New Thermodynamic Equilibrium  
549 Model for Multiphase Multicomponent Inorganic Aerosols, *Aquat. Geochem.*, 4(1), 123–  
550 152, doi:10.1023/A:1009604003981, 1998.

551 Odum, J. R., Hoffmann, T. and Bowman, F.: Gas/particle partitioning and secondary organic  
552 aerosol yields, *Environ. Sci. Technol.*, 30(8), 2580–2585, doi:10.1021/es950943, 1996.

553 Pankow, J. F.: An absorption model of gas/particle partitioning of organic compounds in the  
554 atmosphere, *Atmos. Environ.*, 28(2), 185–188, doi:10.1016/1352-2310(94)90093-0,  
555 1994.

556 Quan, J., Tie, X., Zhang, Q., Liu, Q., Li, X., Gao, Y. and Zhao, D.: Characteristics of heavy  
557 aerosol pollution during the 2012–2013 winter in Beijing, China, *Atmos. Environ.*, 88(C),  
558 83–89, doi:10.1016/j.atmosenv.2014.01.058, 2014.

559 Robinson, A. L., Donahue, N. M., Shrivastava, M. K., Weitkamp, E. A., Sage, A. M.,  
560 Grieshop, A. P., Lane, T. E., Pierce, J. R. and Pandis, S. N.: Rethinking organic aerosols:  
561 semivolatile emissions and photochemical aging, *Science*, 315(5816), 1259–1262,  
562 doi:10.1126/science.1133061, 2007.

563 Seinfeld, J. H. and Pandis, S. N.: *Atmospheric Chemistry and Physics - From Air Pollution to*  
564 *Climate Change*, 2nd ed., John Wiley & Sons, New Jersey. 2006.

565 Shrivastava, M. K., Lane, T. E., Donahue, N. M., Pandis, S. N. and Robinson, A. L.: Effects  
566 of gas particle partitioning and aging of primary emissions on urban and regional organic  
567 aerosol concentrations, *J. Geophys. Res.*, 113(D18), D18301–16,  
568 doi:10.1029/2007JD009735, 2008.

569 Shrivastava, M. K., Lipsky, E. M., Stanier, C. O. and Robinson, A. L.: Modeling  
570 Semivolatile Organic Aerosol Mass Emissions from Combustion Systems, *Environ. Sci.*  
571 *Technol.*, 40(8), 2671–2677, doi:10.1021/es0522231, 2006.

572 Sun, Y. L., Wang, Z. F., Fu, P. Q., Yang, T., Jiang, Q., Dong, H. B., Li, J. and Jia, J. J.:  
573 Aerosol composition, sources and processes during wintertime in Beijing, China, *Atmos.*  
574 *Chem. Phys.*, 13(9), 4577–4592, doi:10.5194/acp-13-4577-2013, 2013.

575 Sun, Y., Wang, Z., Dong, H., Yang, T., Li, J., Pan, X., Chen, P. and Jayne, J. T.:  
576 Characterization of summer organic and inorganic aerosols in Beijing, China with an  
577 Aerosol Chemical Speciation Monitor, *Atmos. Environ.*, 51(C), 250–259,  
578 doi:10.1016/j.atmosenv.2012.01.013, 2012.

579 Tie, X., Huang, R.-J., Dai, W., Cao, J., Long, X., Su, X., Zhao, S., Wang, Q. and Li, G.:  
580 Effect of heavy haze and aerosol pollution on rice and wheat productions in China, *Sci.*  
581 *Rep.*, 1–6, doi:10.1038/srep29612, 2016.

582 Tie, X., Madronich, S., Walters, S., Zhang, R., Rasch, P. and Collins, W.: Effect of clouds on

583 photolysis and oxidants in the troposphere, *J. Geophys. Res.*, 108(D20), 4642,  
584 doi:10.1029/2003JD003659, 2003.

585 Tsimpidi, A. P., Karydis, V. A. and Zavala, M.: Evaluation of the volatility basis-set  
586 approach for the simulation of organic aerosol formation in the Mexico City  
587 metropolitan area, *Atmos. Chem. Phys.*, 10(2), 525–546, doi:10.5194/acp-10-525-2010,  
588 2010.

589 Volkamer, R., San Martini, F., Molina, L. T., Salcedo, D., Jimenez, J. L. and Molina, M. J.:  
590 A missing sink for gas-phase glyoxal in Mexico City: Formation of secondary organic  
591 aerosol, *Geophys. Res. Lett.*, 34(19), L19807, doi:10.1029/2007GL030752, 2007.

592 Wang, G., Zhang, R., Gomez, M. E., Yang, L., Levy Zamora, M., Hu, M., Lin, Y., Peng, J.,  
593 Guo, S., Meng, J., Li, J., Cheng, C., Hu, T., Ren, Y., Wang, Y., Gao, J., Cao, J., An, Z.,  
594 Zhou, W., Li, G., Wang, J., Tian, P., Marrero-Ortiz, W., Secret, J., Du, Z., Zheng, J.,  
595 Shang, D., Zeng, L., Shao, M., Wang, W., Huang, Y., Wang, Y., Zhu, Y., Li, Y., Hu, J.,  
596 Pan, B., Cai, L., Cheng, Y., Ji, Y., Zhang, F., Rosenfeld, D., Liss, P. S., Duce, R. A.,  
597 Kolb, C. E. and Molina, M. J.: Persistent sulfate formation from London Fog to Chinese  
598 haze, *Proc. Natl. Acad. Sci. U.S.A.*, 201616540–18, doi:10.1073/pnas.1616540113,  
599 2016a.

600 Wang, Y., Khalizov, A., Levy, M. and Zhang, R.: New Directions: Light absorbing aerosols  
601 and their atmospheric impacts, *Atmos. Environ.*, 81(C), 713–715,  
602 doi:10.1016/j.atmosenv.2013.09.034, 2013.

603 Wang, Y., Ma, P.-L., Jiang, J. H., Su, H. and Rasch, P. J.: Toward reconciling the influence  
604 of atmospheric aerosols and greenhouse gases on light precipitation changes in Eastern  
605 China, *J. Geophys. Res.*, 121(10), 5878–5887, doi:10.1002/2016JD024845, 2016b.

606 Wang, Y., Ma, P.-L., Peng, J., Zhang, R., Jiang, J. H., Easter, R. C. and Yung, Y. L.:  
607 Constraining Aging Processes of Black Carbon in the Community Atmosphere Model  
608 Using Environmental Chamber Measurements, *J. Adv. Model. Earth Syst.*, 10(10),  
609 2514–2526, doi:10.1029/2018MS001387, 2018.

610 Wei, S., Shen, G., Zhang, Y., Xue, M., Xie, H., Lin, P., Chen, Y., Wang, X. and Tao, S.:  
611 Field measurement on the emissions of PM, OC, EC and PAHs from indoor crop straw  
612 burning in rural China, *Environ. Pollut.*, 184, 18–24, doi:10.1016/j.envpol.2013.07.036,  
613 2014.

614 Wesely, M. L.: Parameterization of surface resistances to gaseous dry deposition in  
615 regional-scale numerical models, *Atmos. Environ.* (1967), 23(6), 1293–1304,  
616 doi:10.1016/0004-6981(89)90153-4, 1989.

617 Wiedinmyer, C., Akagi, S. K., Yokelson, R. J., Emmons, L. K., Al-Saadi, J. A., Orlando, J. J.  
618 and Soja, A. J.: The Fire INventory from NCAR (FINN): a high resolution global model  
619 to estimate the emissions from open burning, *Geoscientific Model Development*, 4(3),  
620 625–641, doi:10.5194/gmd-4-625-2011, 2011.

621 Wiedinmyer, C., Quayle, B., Geron, C., Belote, A., McKenzie, D., Zhang, X., O'Neill, S. and  
622 Wynne, K. K.: Estimating emissions from fires in North America for air quality  
623 modeling, *Atmos. Environ.*, 40(19), 3419–3432, doi:10.1016/j.atmosenv.2006.02.010,  
624 2006.

625 Wu, J., Li, G., Cao, J., Bei, N., Wang, Y., Feng, T., Huang, R., Liu, S., Zhang, Q. and Tie, X.:  
626 Contributions of trans-boundary transport to summertime air quality in Beijing, China,  
627 *Atmos. Chem. Phys.*, 17(3), 2035–2051, doi:10.5194/acp-17-2035-2017, 2017.

628 Xing, L., Wu, J., Elser, M., Tong, S., Liu, S., Li, X., Liu, L., Cao, J., Zhou, J., Haddad, El, I.,  
629 Huang, R., Ge, M., Tie, X., Prévôt, A. S. H. and Li, G.: Wintertime secondary organic  
630 aerosol formation in Beijing–Tianjin–Hebei (BTH): contributions of HONO sources and  
631 heterogeneous reactions, *Atmos. Chem. Phys.*, 19(4), 2343–2359,  
632 doi:10.5194/acp-19-2343-2019, 2019.

633 Zhang, Q., Jimenez, J. L., Canagaratna, M. R., Allan, J. D., Coe, H., Ulbrich, I., Alfarra, M.  
634 R., Takami, A., Middlebrook, A. M., Sun, Y. L., Dzepina, K., Dunlea, E., Docherty, K.,  
635 DeCarlo, P. F., Salcedo, D., Onasch, T., Jayne, J. T., Miyoshi, T., Shimojo, A.,  
636 Hatakeyama, S., Takegawa, N., Kondo, Y., Schneider, J., Drewnick, F., Borrmann, S.,  
637 Weimer, S., Demerjian, K., Williams, P., Bower, K., Bahreini, R., Cottrell, L., Griffin, R.  
638 J., Rautiainen, J., Sun, J. Y., Zhang, Y. M. and Worsnop, D. R.: Ubiquity and dominance  
639 of oxygenated species in organic aerosols in anthropogenically-influenced Northern  
640 Hemisphere midlatitudes, *Geophys. Res. Lett.*, 34(13), L13801,  
641 doi:10.1029/2007GL029979, 2007.

642 Zhang, Q., Streets, D. G. and Carmichael, G. R.: Asian emissions in 2006 for the NASA  
643 INTEX-B mission, *Atmos. Chem. Phys.*, 9(14), 5131–5153,  
644 doi:10.5194/acp-9-5131-2009, 2009.

645 Zhao, J., Levitt, N. P., Zhang, R. and Chen, J.: Heterogeneous Reactions of Methylglyoxal in  
646 Acidic Media: Implications for Secondary Organic Aerosol Formation, *Environ. Sci.*  
647 *Technol.*, 40(24), 7682–7687, doi:10.1021/es060610k, 2006.

648 Zhou, X., Bei, N., Liu, H., Cao, J., Xing, L., Lei, W., Molina, L. T. and Li, G.: Aerosol  
649 effects on the development of cumulus clouds over the Tibetan Plateau, *Atmos. Chem.*  
650 *Phys.*, 17(12), 7423–7434, doi:10.5194/acp-17-7423-2017, 2017.

651  
652  
653  
654  
655

656 Table 1 Anthropogenic emissions of various species in the simulation domain in October  
657 2015 (Unit: Mton month<sup>-1</sup>)  
658

Species	NO <sub>x</sub>	SO <sub>2</sub>	NH <sub>3</sub>	CO	VOC	OC	EC
Beijing	0.31	0.02	0.05	0.66	1.51	0.03	0.01
Tianjin	0.24	0.09	0.05	0.09	2.8	0.05	0.01
Hebei	2.21	0.7	0.62	3.59	21.59	0.41	0.06
Domain	14.21	7.1	4.45	22.19	124.71	2.56	0.3

659  
660  
661  
662  
663

664 Table 2 WRF-Chem model configuration  
 665

Item	Configuration
Period	3 ~ 8 October 2015
Regions	Beijing-Tianjin-Hebei, China
Domain center	116°E, 38°N
Domain size	1200 km × 1200 km
Horizontal resolution	6 km × 6 km
Vertical resolution	35 vertical levels with a stretched vertical grid with spacing ranging from 50 m near surface, to 500 m at 2.5 km and 1 km above 14 km
Microphysics scheme	WRF Single-Moment 6-class scheme (Hong and Lim, 2006)
Boundary layer scheme	MYJ TKE scheme (Janjić, 2002)
Surface layer scheme	MYJ surface scheme (Janjić, 2002)
Land-surface scheme	Noah land surface model (Chen and Dudhia, 2001)
Longwave radiation scheme	New Goddard scheme (Chou et al., 2001)
Shortwave radiation scheme	New Goddard scheme (Chou and Suarez, 1999)
Meteorological boundary and initial condition	NCEP 1° × 1° reanalysis data
Chemical boundary and initial condition	MOZART 6-h output (Horowitz et al., 2003)
Anthropogenic emission inventory	SAPRC99 chemical mechanism emissions (Zhang et al., 2009), base year: 2013
Biogenic emission inventory	MEGAN model developed by Guenther et al. (2006)
Spin-up time	1.5 days

666  
 667  
 668  
 669  
 670



671 Table 3 Description of the reference simulation and sensitivity experiments  
672

Case ID	Description
REF	The reference simulation constrained by observations
SEN1	10% decrease in photolysis frequencies
SEN2	20% decrease in photolysis frequencies
SEN3	30% decrease in photolysis frequencies
SEN4	40% decrease in photolysis frequencies

673  
674  
675  
676  
677

678

## Figure captions

679

680 Figure 1 Model domain with the topography. The black circles denote the locations of the  
681 cities with ambient air quality monitoring sites, and the size of the circles represents  
682 the number of sites in each city. The white triangles show the location of the  
683 meteorological stations in Beijing, Tianjin, Shijiazhuang, and Baoding. The light blue  
684 and pink dots in Beijing show the observation sites with the POA/SOA (NCNT) and  
685 OC/EC (CRAES) measurements, respectively.

686 Figure 2 Geographic distributions of anthropogenic emissions of (a) volatile organic  
687 compounds and (b) organic carbon in October in the simulation domain. The black  
688 lines present provincial boundaries in China.

689 Figure 3 (a) Measured concentrations of O<sub>3</sub>, NO<sub>2</sub>, SO<sub>2</sub>, CO, and PM<sub>2.5</sub> in BTH averaged  
690 during 15 September ~ 14 November from 2013 to 2017, and (b) OC and EC  
691 concentrations (bars) and OC/EC ratios (line) measured in Beijing averaged during 15  
692 September ~ 14 November from 2013 to 2015.

693 Figure 4 Simulated (red curves) and observed (black dots) temporal profiles of surface (a-d)  
694 temperature and (e-h) relative humidity in (a, e) Beijing, (b, f) Tianjin, (c, g)  
695 Shijiazhuang, and (d, h) Baoding from 3 to 8 October 2015.

696 Figure 5 Simulated (red curves) and observed (black dots) temporal profiles of surface (a-d)  
697 wind speed and (e-h) wind direction in (a, e) Beijing, (b, f) Tianjin, (c, g)  
698 Shijiazhuang, and (d, h) Baoding from 3 to 8 October 2015.

699 Figure 6 Spatial distributions of the modeled (colored shadings) and observed (colored dots)  
700 surface daily PM<sub>2.5</sub> concentration from 3 to 8 October 2015. Black arrows show the  
701 simulated surface winds.

702 Figure 7 Spatial distributions of the modeled (colored shadings) and observed (colored dots)  
703 surface O<sub>3</sub> concentration at 14:00 (local time) from 3 to 8 October 2015. Black arrows  
704 show the simulated surface winds.

705 Figure 8 Diurnal variations of the modeled (red curves) and observed (black dots) surface (a)  
706 PM<sub>2.5</sub>, (b) O<sub>3</sub>, and (c) NO<sub>2</sub> concentrations averaged over 12 ambient monitoring  
707 stations in Beijing from 3 to 8 October 2015.

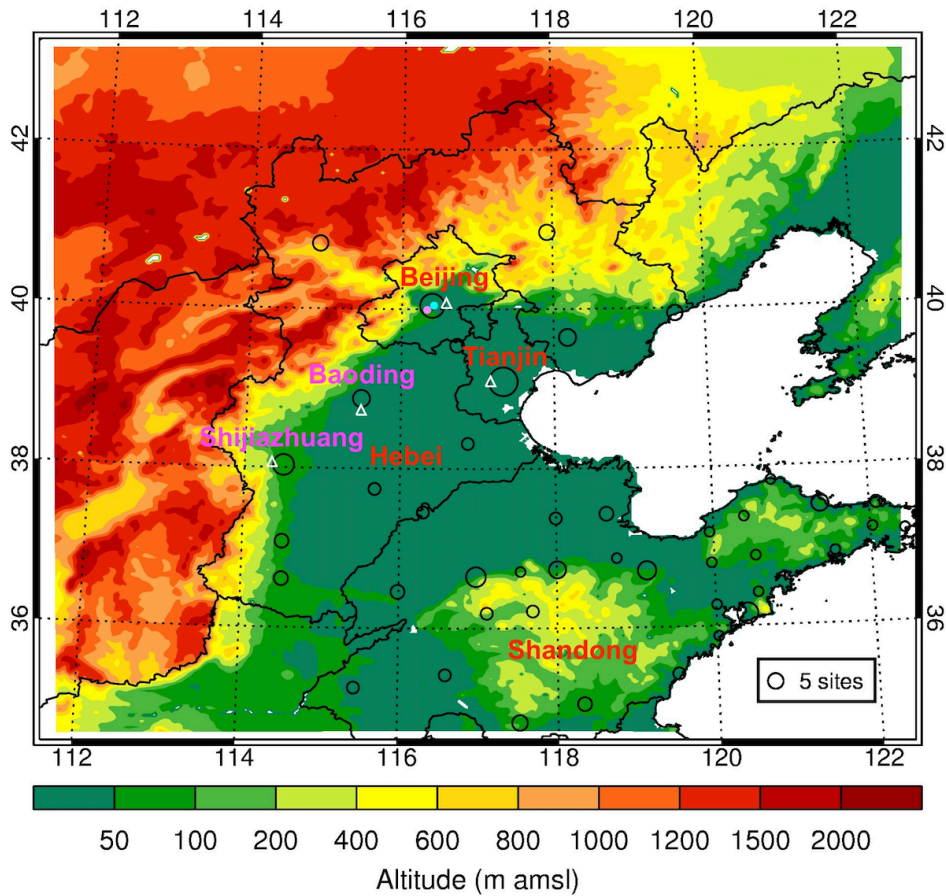
708 Figure 9 Diurnal variations of the modeled (red curves) and observed (black dots) surface  
709 submicron (a) POA and (b) SOA concentrations at the NCNT station, and (c) EC  
710 concentration in PM<sub>2.5</sub> at the CRAES station in Beijing from 3 to 8 October 2015.

711 Figure 10 Impacts of changes in the AOC on organic aerosol components in BTH in 4  
712 sensitivity experiments. (a) Concentration changes of POA, SOA, and TOA *versus* O<sub>3</sub>,  
713 (b) Concentration changes of POA, SOA, and TOA *versus* OH, (c) SOA fraction in  
714 TOA *versus* OH concentration change, and (d) OC/EC ratio *versus* OH concentration  
715 change.

716 Figure 11 Spatial distributions of changes in (a, c) OH and (b, d) SOA concentrations  
717 averaged from 4 to 7 October 2015 in the SEN3 experiment compared to the REF  
718 simulation (SEN3 – REF).

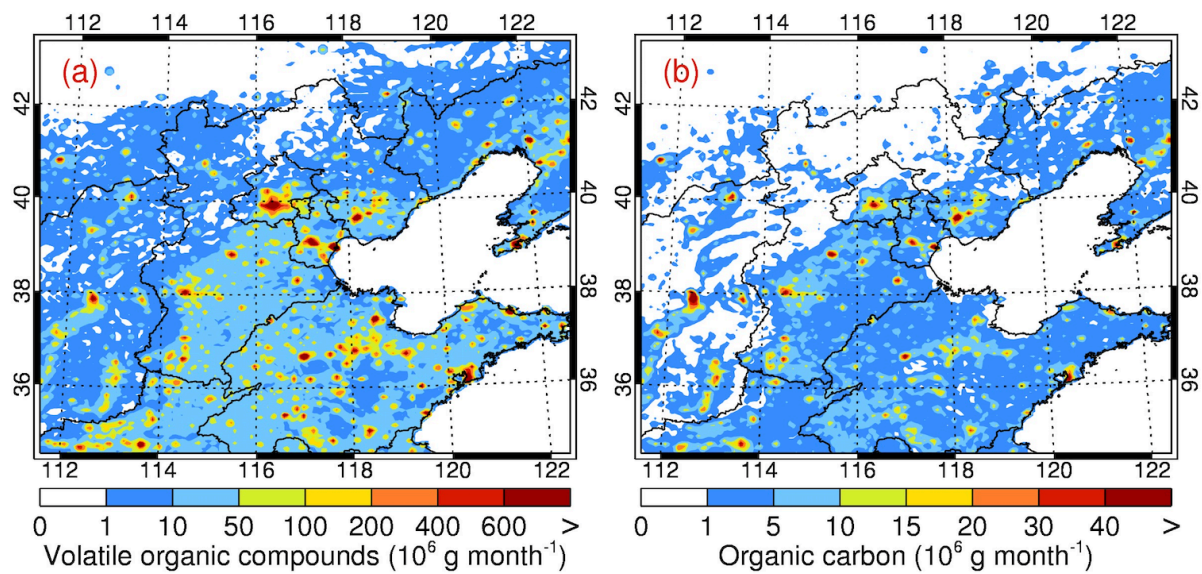
719 Figure 12 Histogram showing the decreases of SOA from various pathways in (a, b) Beijing,  
720 (c, d) Tianjin, and (e, f) Hebei in the sensitivity experiments compared to the REF  
721 simulation ( $SEN_x - REF$ ,  $x = 1, 2, 3,$  and  $4$ ). PSOA: oxidation and partitioning of  
722 semivolatile POA and co-emitted IVOCs; ASOA: oxidation and partitioning of  
723 anthropogenic VOCs; BSOA: oxidation and partitioning of biogenic VOCs; HSOA:  
724 heterogeneous reactions of glyoxal and methylglyoxal on aerosol surfaces.

725  
726  
727  
728  
729



730  
 731  
 732  
 733  
 734  
 735  
 736  
 737  
 738  
 739  
 740  
 741  
 742

Figure 1 Model domain with the topography. The black circles denote the locations of the cities with ambient air quality monitoring sites, and the size of the circles represents the number of sites in each city. The white triangles show the location of the meteorological stations in Beijing, Tianjin, Shijiazhuang, and Baoding. The light blue and pink dots in Beijing show the observation sites with the POA/SOA (NCNT) and OC/EC (CRAES) measurements, respectively.

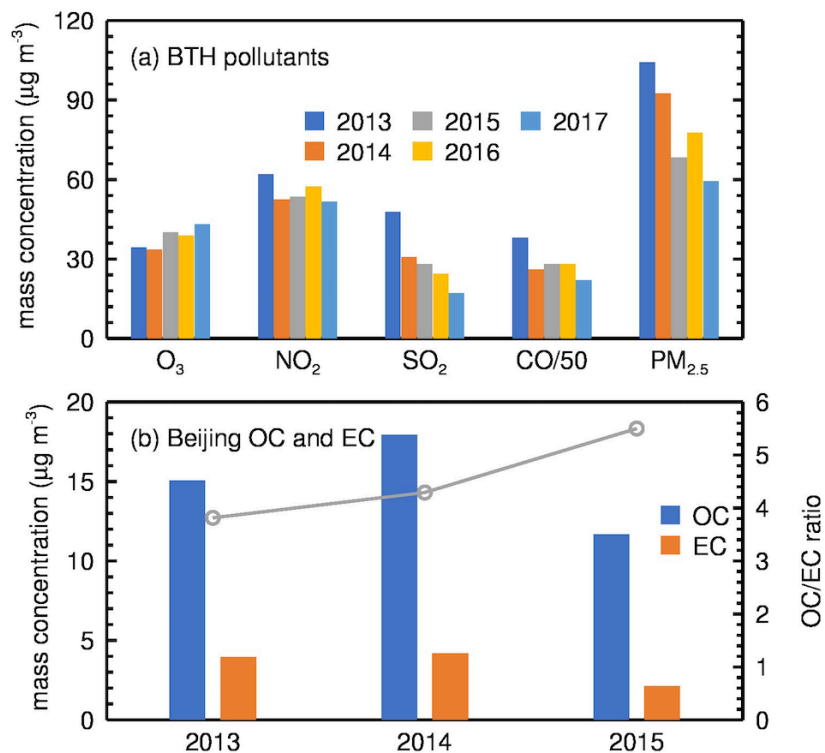


743

744

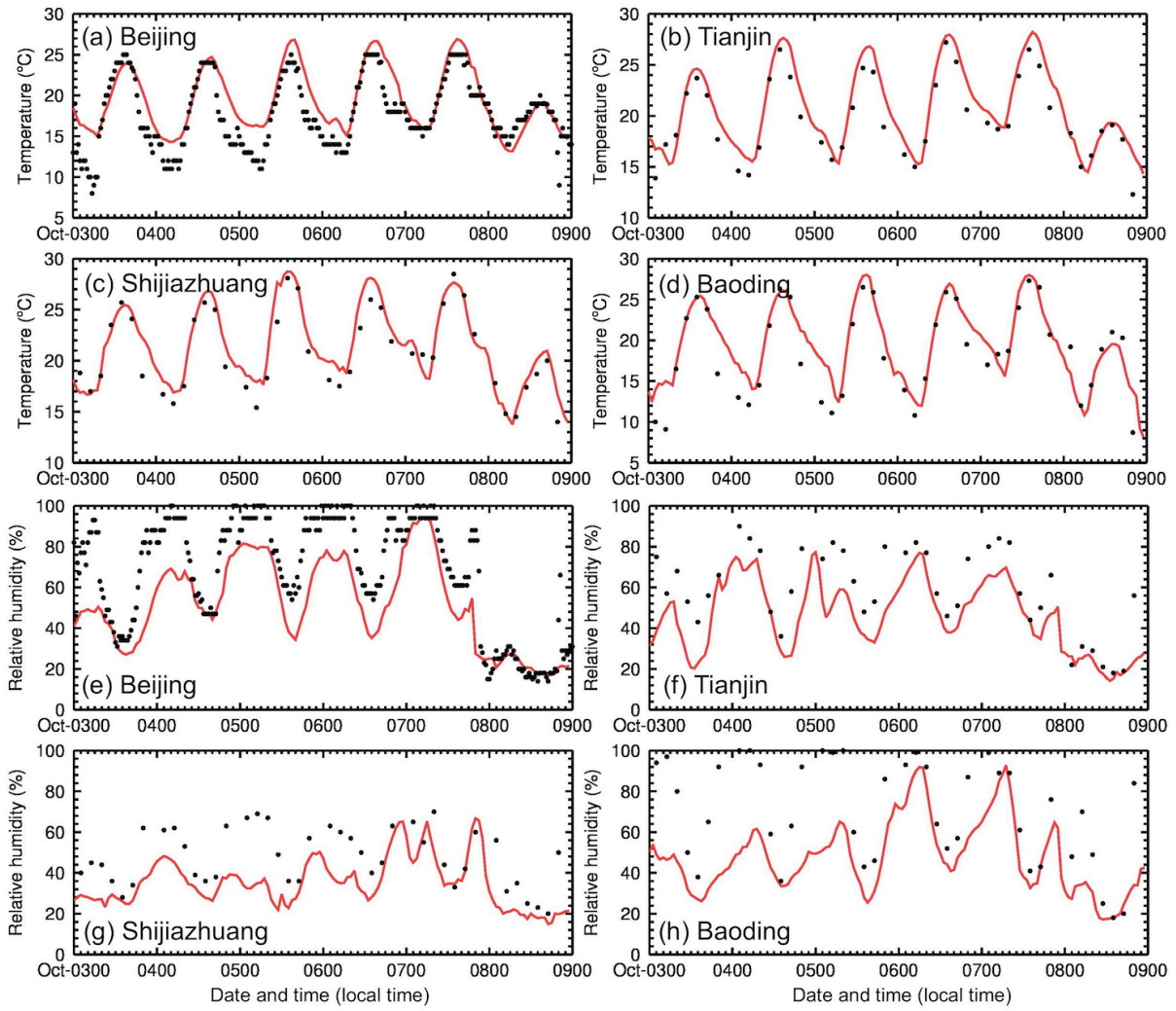
745 Figure 2 Geographic distributions of anthropogenic emissions of (a) volatile organic  
 746 compounds and (b) organic carbon in October in the simulation domain. The black lines  
 747 present provincial boundaries in China.

748



749  
 750  
 751  
 752  
 753  
 754  
 755  
 756  
 757  
 758  
 759

Figure 3 (a) Measured concentrations of O<sub>3</sub>, NO<sub>2</sub>, SO<sub>2</sub>, CO, and PM<sub>2.5</sub> in BTH averaged during 15 September ~ 14 November from 2013 to 2017, and (b) OC and EC concentrations (bars) and OC/EC ratios (line) measured in Beijing averaged during 15 September ~ 14 November from 2013 to 2015.



760

761

762 Figure 4 Simulated (red lines) and observed (black dots) temporal profiles of surface (a-d)  
 763 temperature and (e-h) relative humidity in (a, e) Beijing, (b, f) Tianjin, (c, g) Shijiazhuang,  
 764 and (d, h) Baoding from 3 to 8 October 2015.

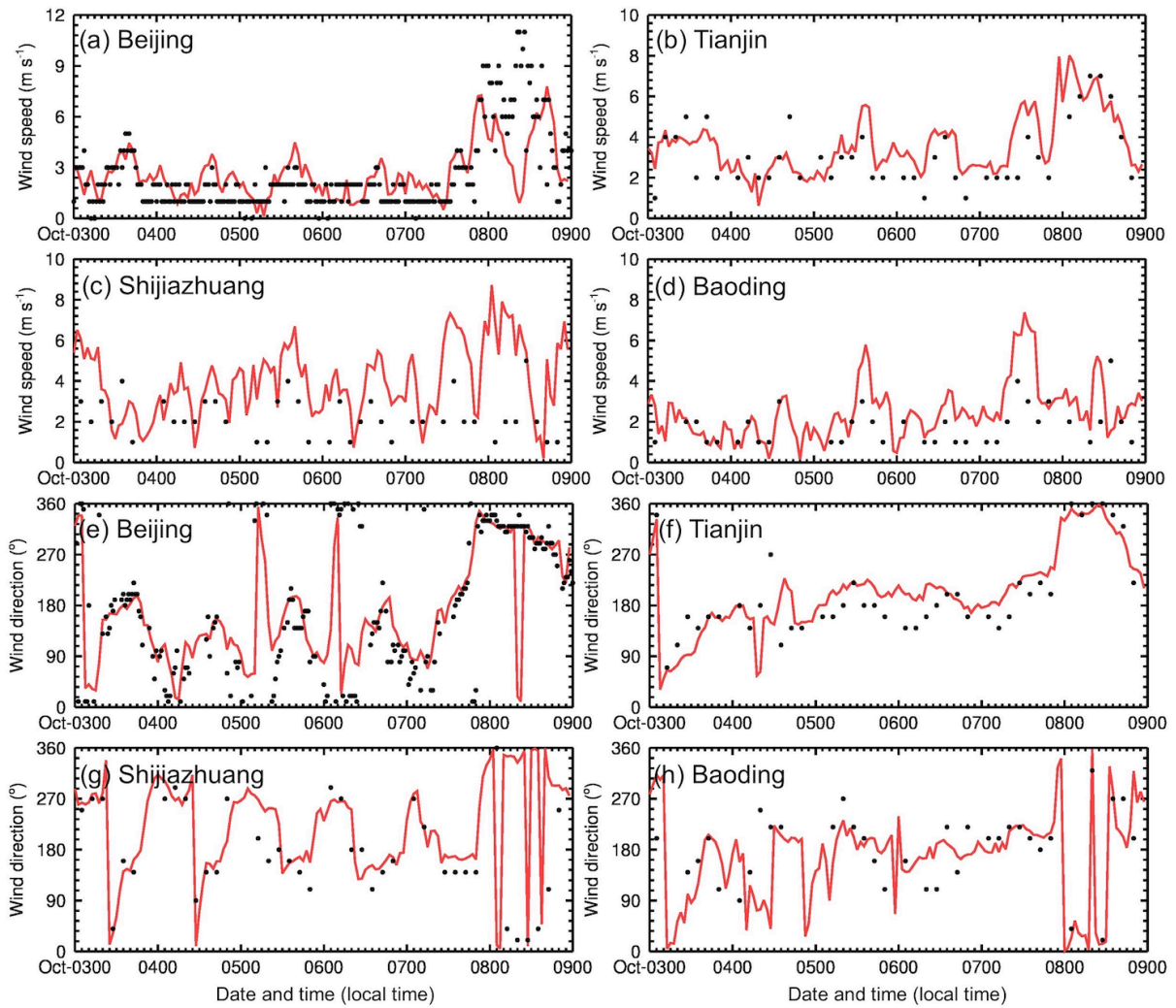
765

766

767

768

769



770

771

772 Figure 5 Simulated (red lines) and observed (black dots) temporal profiles of surface (a-d)  
 773 wind speed and (e-h) wind direction in (a, e) Beijing, (b, f) Tianjin, (c, g) Shijiazhuang, and  
 774 (d, h) Baoding from 3 to 8 October 2015.

775

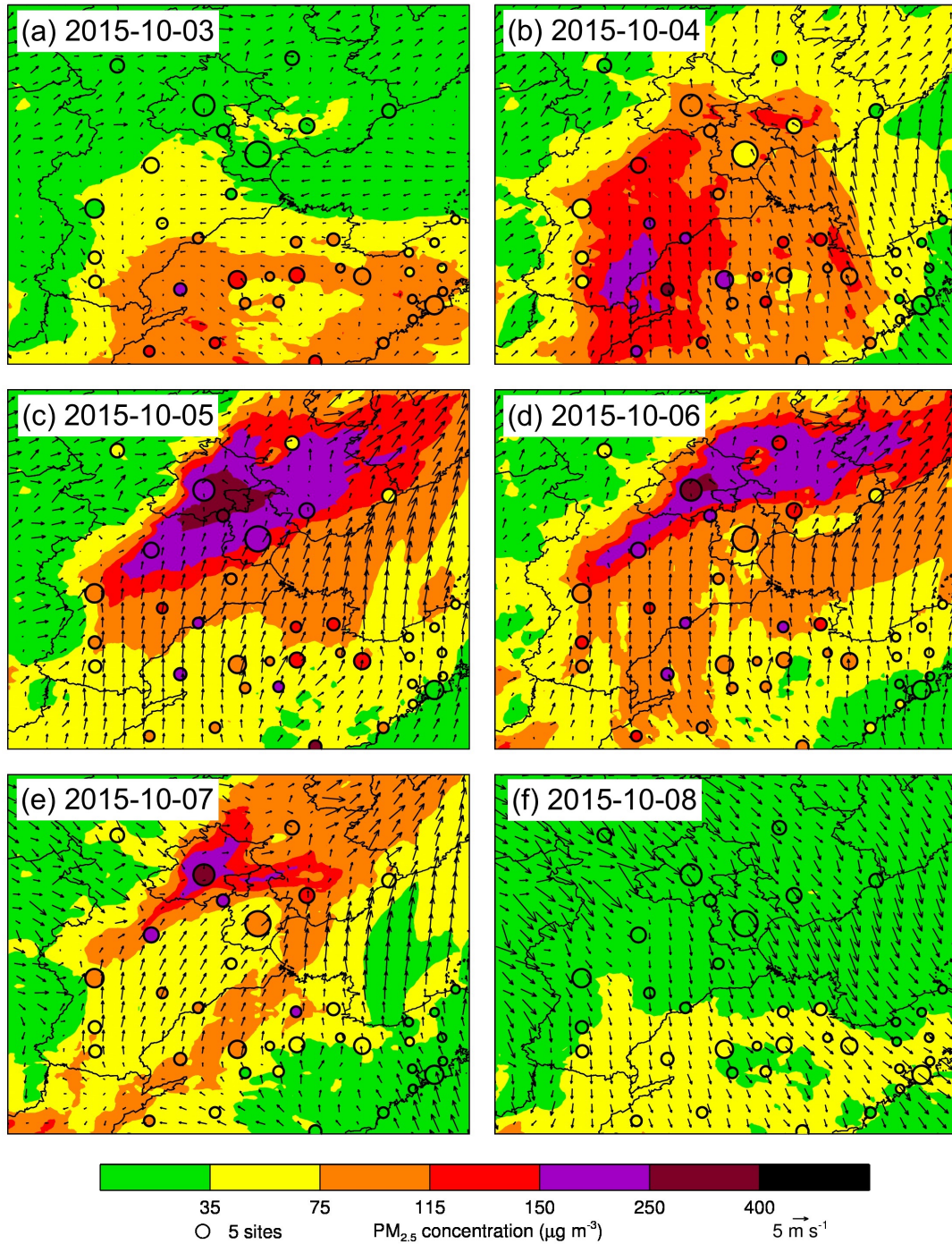
776

777

778

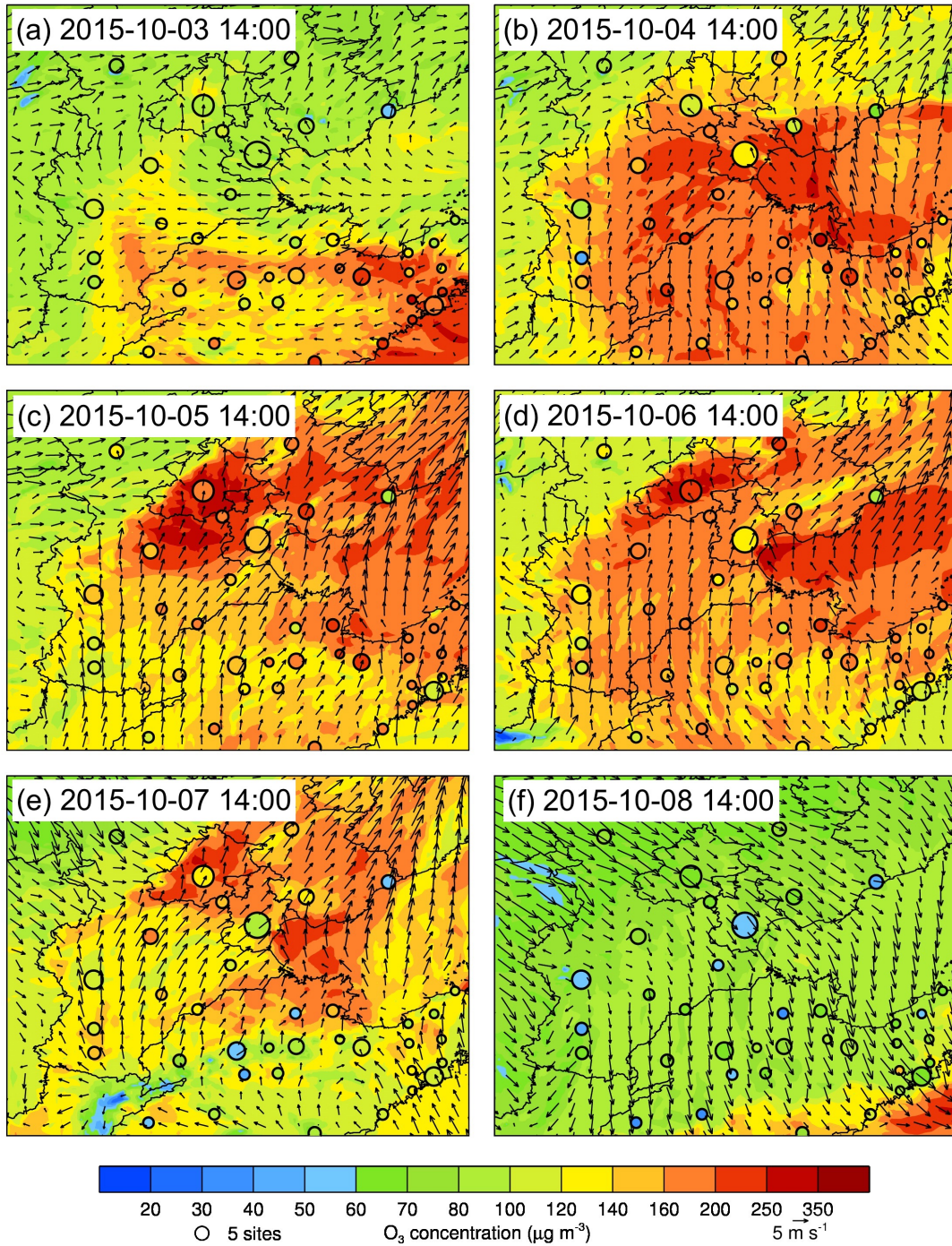
779





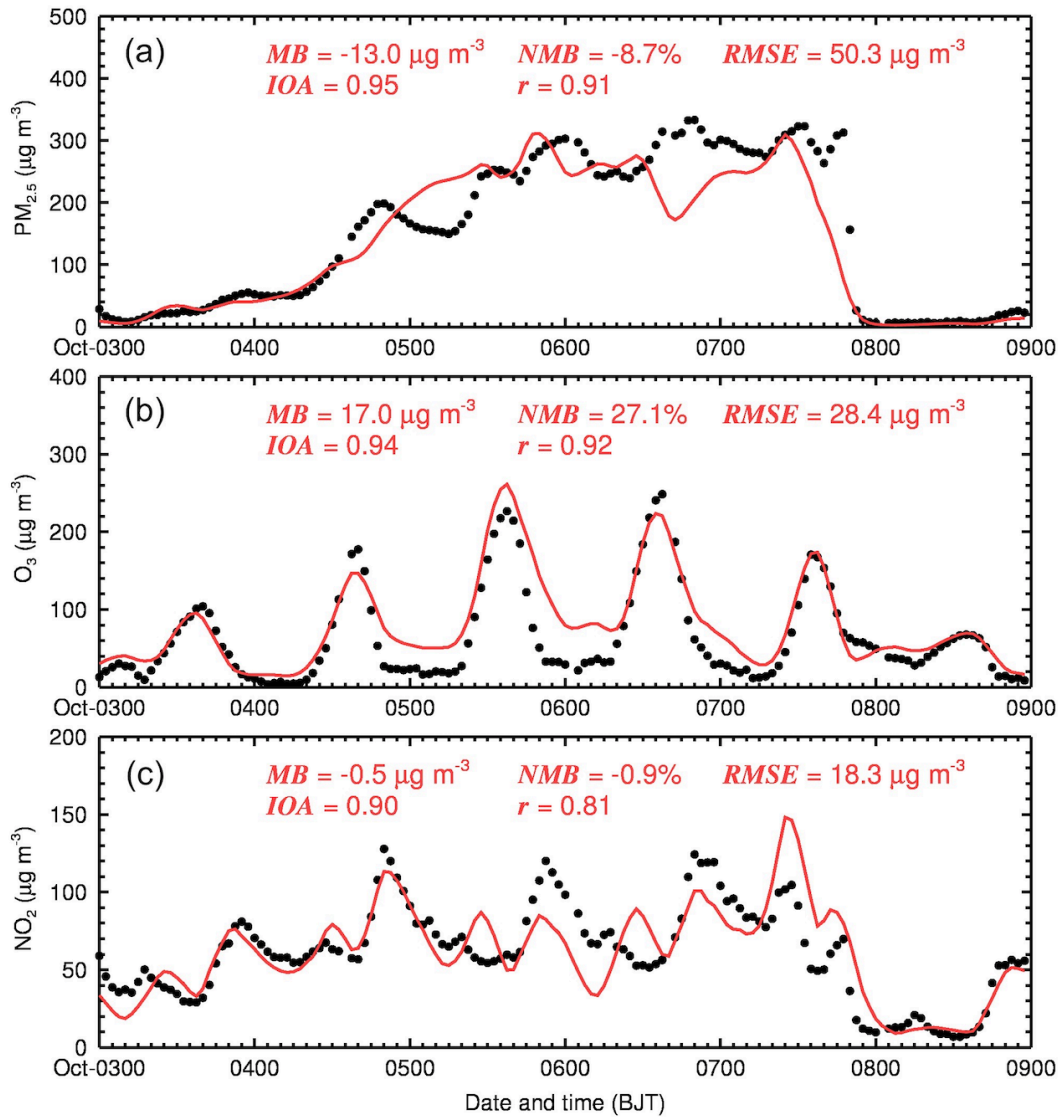
780  
 781  
 782  
 783  
 784  
 785  
 786  
 787  
 788  
 789

Figure 6 Spatial distributions of the modeled (colored shadings) and observed (colored dots) surface daily PM<sub>2.5</sub> concentration from 3 to 8 October 2015. Black arrows show the simulated surface winds.



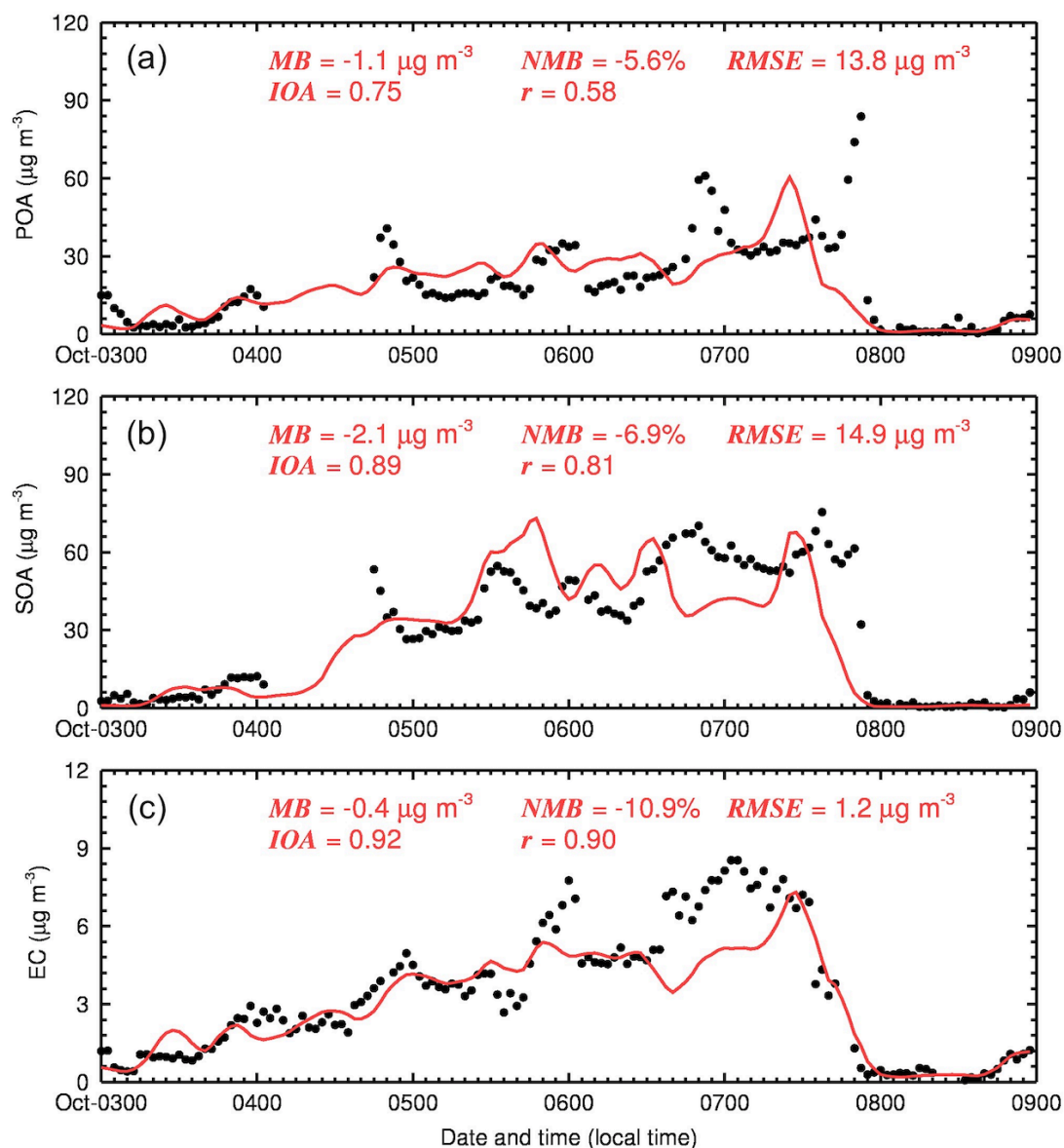
790  
791  
792  
793  
794  
795  
796  
797  
798  
799

Figure 7 Spatial distributions of the modeled (colored shadings) and observed (colored dots) surface O<sub>3</sub> concentration at 14:00 (local time) from 3 to 8 October 2015. Black arrows show the simulated surface winds.



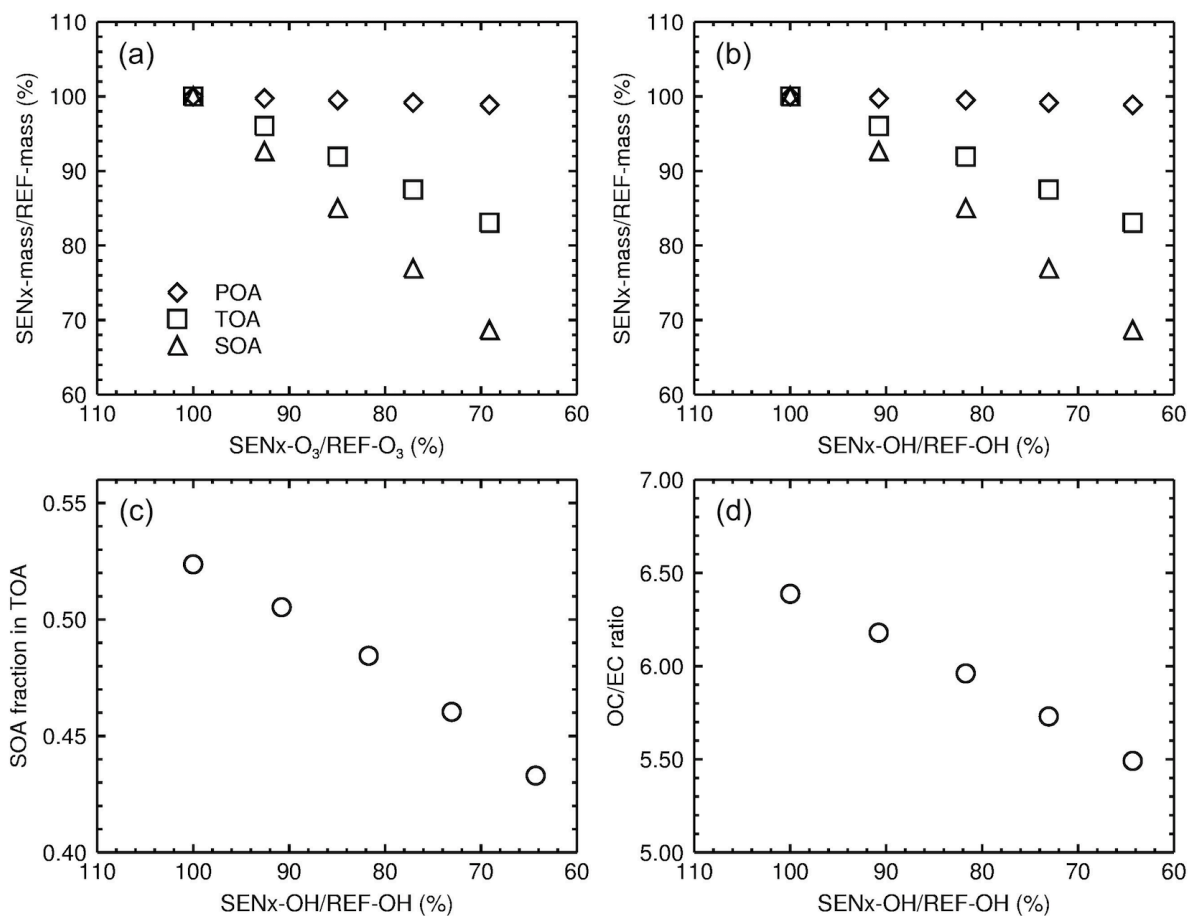
800  
 801  
 802  
 803  
 804  
 805  
 806  
 807  
 808  
 809

Figure 8 Diurnal variations of the modeled (red curves) and observed (black dots) surface (a)  $\text{PM}_{2.5}$ , (b)  $\text{O}_3$ , and (c)  $\text{NO}_2$  concentrations averaged over 12 ambient monitoring stations in Beijing from 3 to 8 October 2015.



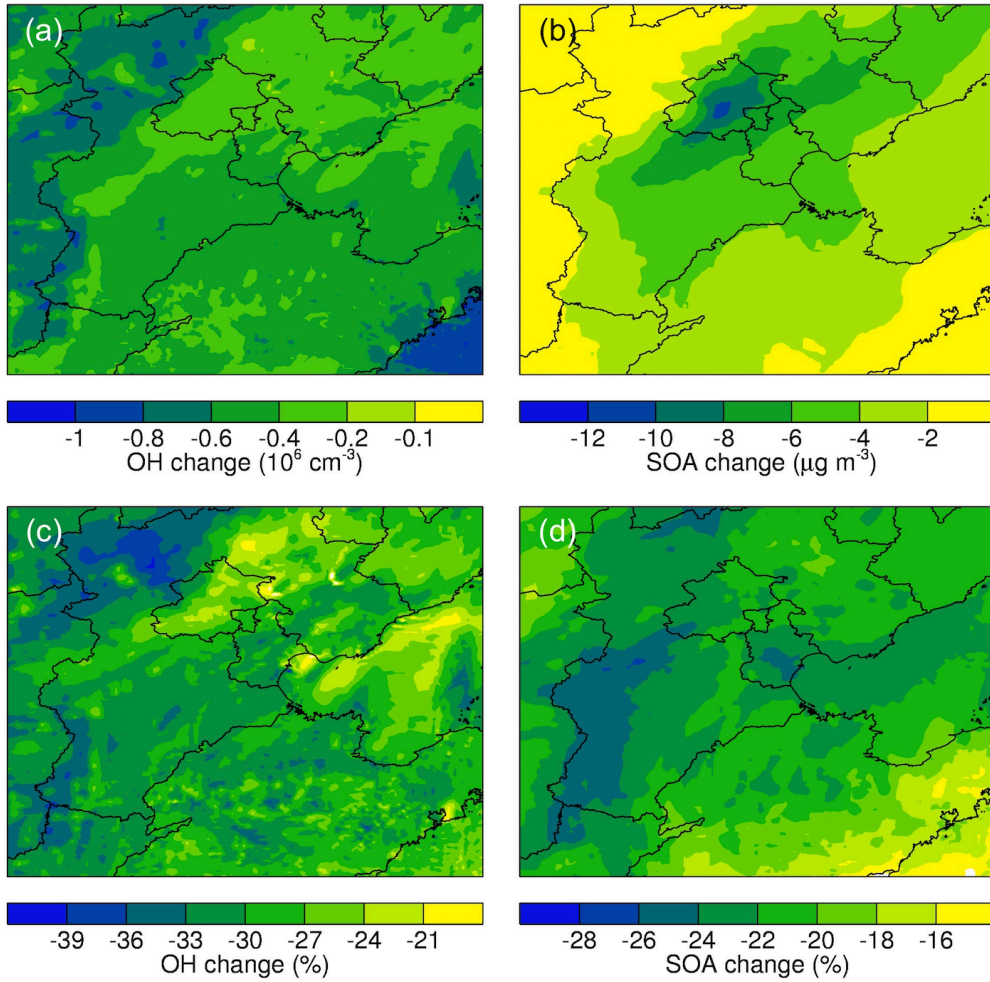
810  
811  
812  
813  
814  
815  
816  
817  
818  
819

Figure 9 Diurnal variations of the modeled (red curves) and observed (black dots) surface submicron (a) POA and (b) SOA concentrations at the NCNT station, and (c) EC concentration in  $\text{PM}_{2.5}$  at the CRAES station in Beijing from 3 to 8 October 2015.



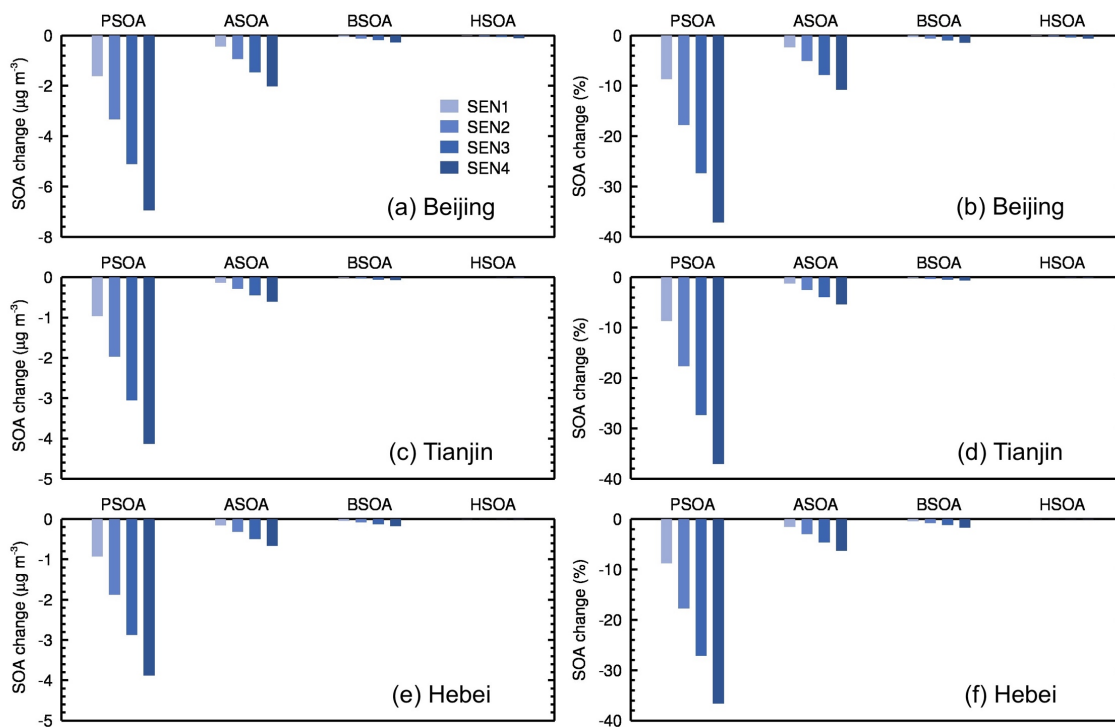
820  
 821  
 822  
 823  
 824  
 825  
 826  
 827  
 828  
 829  
 830

Figure 10 Impacts of changes in the AOC on organic aerosol components in BTH in 4 sensitivity experiments. (a) Concentration changes of POA, SOA, and TOA *versus* O<sub>3</sub>, (b) Concentration changes of POA, SOA, and TOA *versus* OH, (c) SOA fraction in TOA *versus* OH concentration change, and (d) OC/EC ratio *versus* OH concentration change.



831  
 832  
 833  
 834  
 835  
 836  
 837  
 838  
 839  
 840

Figure 11 Spatial distributions of changes in (a, c) OH and (b, d) SOA concentrations averaged from 4 to 7 October 2015 in the SEN3 experiment compared to the REF simulation (SEN3 – REF).



841  
842

843 Figure 12 Histogram showing the decreases of SOA from various pathways in (a, b) Beijing,  
844 (c, d) Tianjin, and (e, f) Hebei in the sensitivity experiments compared to the REF simulation  
845 (SEN<sub>x</sub> – REF, x = 1, 2, 3, and 4). PSOA: oxidation and partitioning of semivolatile POA and  
846 co-emitted IVOCs; ASOA: oxidation and partitioning of anthropogenic VOCs; BSOA:  
847 oxidation and partitioning of biogenic VOCs; HSOA: heterogeneous reactions of glyoxal and  
848 methylglyoxal on aerosol surfaces.

849

850

851

852